ISTANBUL TECHNICAL UNIVERSITY ★ GRADUATE SCHOOL

DATING AND INTERPRETING A FIRN CORE FROM THE EAST ANTARCTIC PLATEAU

M.Sc. THESIS

Furkan Kaan SAĞOL

Department of Solid Earth Sciences

Geodynamics Programme

AUGUST 2024

ISTANBUL TECHNICAL UNIVERSITY ★ GRADUATE SCHOOL

DATING AND INTERPRETING A FIRN CORE FROM THE EAST ANTARCTIC PLATEAU

M.Sc. THESIS

Furkan Kaan SAĞOL
(602201003)

Department of Solid Earth Sciences

Geodynamics Programme

Thesis Advisor: Asst. Prof. Dr. Georg SCHWAMBORN
Thesis Co-Advisor: Asst. Prof. Dr. Maria HÖRHOLD

AUGUST 2024

ISTANBUL TEKNİK ÜNİVERSİTESİ ★ LİSANSÜSTÜ EĞİTİM ENSTİTÜSÜ

DOĞU ANTARKTİKA PLATOSU'NDAN ALINAN FIRN KAROTUNUN TARİHLENDİRİLMESİ VE YORUMLANMASI

YÜKSEK LİSANS TEZİ

Furkan Kaan SAĞOL
(602201003)

Katı Yer Bilimleri Ana Bilim Dalı

Jeodinamik Programı

Tez Danışmanı: Dr. Ögr. Üyesi Georg SCHWAMBORN
Eş Danışman: Dr. Ögr. Üyesi Maria HÖRHOLD

AĞUSTOS 2024

Furkan Kaan Sağol, a M.Sc. student of İTU Graduate School student ID 602201003, successfully defended the thesis/dissertation entitled "DATING AND INTERPRETING A FIRN CORE FROM THE EAST ANTARCTIC PLATEAU", which he prepared after fulfilling the requirements specified in the associated legislations, before the jury whose signatures are below.

Thesis Advisor :	**Asst. Prof. Dr. Georg SCHWAMBORN** Istanbul Technical University	.....
Co-advisor :	**Asst. Prof. Dr. Maria HÖRHOLD** Alfred Wegener Institute	.....
Jury Members :	**Asst. Prof. Dr. Ali MOHAMMADİ** Istanbul Technical University	.....
	Prof. Dr. Mehmet KARACA Istanbul Technical University	.....
	Assoc. Prof. Dr. Özlem MAKAROĞLU Istanbul University-Cerrahpaşa	.....

Date of Submission : 22 May 2024
Date of Defense : 29 August 2024

FOREWORD

I am very excited and proud to announce the completion of my thesis titled “Dating and Interpreting a Firn Core from the East Antarctic Plateau”. This research, conducted at the Alfred-Wegener-Institut (AWI), provided me with unique and valuable knowledge in the field of glaciology and was an extraordinary experience in my academic journey. I would like to express my deep gratitude to my valuable advisors, Dr. Georg J. Schwamborn and Dr. Maria Hörhold, for giving me access to this comprehensive knowledge and for their valuable guidance and support. Additionally, I would like to extend my gratitudes to Dr. Johannes Freitag, Prof. Dr. Frank Wilhelms, Dr. Sepp Kipfstuhl, and Dr. Coen Hofstede, who shared their knowledge and experience with me during my work at AWI.

I am also grateful to Dr. Metin Baykara, who helped me improve my Python programming skills, and to my friends who were always by my side.

One of the most important contributions to the realization of my thesis work was the project budget provided by the Scientific Research Projects (İTÜ-BAP) Unit of Istanbul Technical University. Therefore, I am very grateful to the İTÜ-BAP unit for supporting my master’s thesis project code “TYL-2022-43643”.

Finally, I would like to thank the Istanbul Technical University Foundation (İTÜ Vakfı) for their financial support, which ensured the sustainability of my research, and my esteemed professor, Prof. Dr. Mehmet Karaca.

May 2024

Furkan Kaan SAĞOL
(Engineer)

TABLE OF CONTENTS

Page

ABBREVIATIONS

ACC : Antarctic Circumpolar Current
APIS : Antarctic Peninsula Ice Sheet
AWI : Alfred Wegener Institute
BCE : Before Common Era
CE : Common Era
CFA : Continuous Flow Analysis
CoFi : Coldest Firn
DEP : Dielectric Profiling
DF2 : Dome Fuji 2
Dome A : Dome Argus
Dome F : Dome Fuji
EAP : East Antarctic Plateau
EAIS : East Antarctic Ice Sheet
EDC : EPICA Dome C
HL model : Herron-Langway Densification Model
NDF : New Dome Fuji
NDFN : New Dome Fuji North
SMOW : Standard Mean Ocean Water
WAIS : West Antarctic Ice Sheet

SYMBOLS

A	**:** Annual mean accumulation rate
CH_4	**:** Methane
CI	**:** Confidence interval
CO_2	**:** Carbon dioxide
D	**:** Deuterium
d	**:** Euclidean distance
Δd	**:** Change in depth
Δt	**:** Time interval between two consecutive measurements
$\delta^{18}O$	**:** Stable oxygen isotope ratios
δD	**:** Stable hydrogen isotope ratios
h_{550}	**:** Depth at the critical density
$h_{m,n}$	**:** Actual depth in metersat the n-th layer
$h_{m,(n-1)}$	**:** Actual depth in meters at the (n-1)-th layer
$h_{w.e.,n}$	**:** Depth in meters water equivalent at the n-th layer
$h_{w.e.,(n-1)}$	**:** Depth in meters water equivalent at the (n-1)-th layer
H	**:** Protium
$J\ K^{-1}\ mol^{-1}$	**:** Joule per kelvin per mole
K	**:** Kelvin
k_0	**:** Rate constant for densification in the first stage
k_1	**:** Rate constant for the densification in the second stage
$kg\ m^{-2}$	**:** Kilogram per square meter
$kg\ m^{-3}$	**:** Kilograms per cubic meter
km	**:** Kilometers
km^2	**:** Square kilometers
km^3	**:** Cubic kilometers
M	**:** Mean
M'	**:** Mean after exclusion
m	**:** Meters
$m\ km^{-1}$	**:** Meters per kilometer
m w.e.	**:** Meters water equivalent

m w.e. year^{-1} : Meter water equivalent per year

Mya : Million years ago

Na^+ : Sodium

NO^{3-} : Nitrate

nssSO_4^{2-} : Non-sea-salt sulfate

^{16}O : Oxygen-16

^{18}O : Oxygen-18

^1H : Protium

^2H : Deuterium

ρ_0 : Initial snow density

ρ_i : Density of ice

ρ_{550} : Critical density

$\rho_{(n-1)}$: Density of the firn at the (n-1)-th layer

ρ_h : Density values, depth profile of densification

R : Gas constant

σ : Standard deviation

σ' : Standard deviation after exclusion

SO_4^{2-} : Sulfate

t_ρ : Time corresponding to a specific density

t_{550} : Age of the critical density

T : Annual mean temperature

± : Plus-minus

Z_0 : Density at specific depths for the first stage of densification

Z_1 : Density at specific depth for the second stage of densification

LIST OF TABLES

Page

LIST OF FIGURES

Page

DATING AND INTERPRETING A FIRN CORE FROM THE EAST ANTARCTIC PLATEAU

SUMMARY

Detecting and understanding potential changes in annual mean temperature and accumulation rate at the East Antarctic Plateau is crucial to assess the sensitivity and future response of the Antarctic ice sheet to global warming. Due to the very low accumulation rate and its spatial variability, the interpretation of climate proxies from shallow firn cores with centennial to decadal time resolution is challenging. A major limitation is the available time resolution obtained by available dating approaches and a reliable assessment of its uncertainty.

In this study, a 204 m long firn core, B56, drilled in 2017 on the East Antarctic Plateau, is analyzed. The major goal of this study is dating the firn core by combining different dating methods based on available density data, dielectric properties, and ion chromatography (of non-sea-salt sulfate) data. To utilize density, the Herron-Langway model is used for determining the depth-age relation. In this model, temperature and snow accumulation are assumed to be constant and the relationship between the snow density and the depth below the snow surface does not change over time. Depending on the accumulation rate used, the resulting age at 200 m depth varies between 6000 to 7200 years. Secondly, the dielectric profile and non-sea-salt sulfate concentration ($nssSO_4^{2-}$) data are used for constructing another depth-age model, thereby matching prominent data peaks to known volcanic eruptions that have been recorded in the past. Here, the resulting age at 200 m depth is determined to be about 6200 years, which compares well to published age models of firn cores from the East Antarctic Plateau. In comparison, it is recognized that all age models are consistent within the upper 40 m (stretching over the past 1000 years), but the Herron-Langway model tends to overestimate the age at greater depths. It is proposed that the findings indicate changes of the accumulation rate in the past, leading to the offset in the Herron-Langway model (which uses a constant accumulation rate).

However, by combining the dating methods, it is possible not only to provide a reasonable dating over the full firn core, but also to improve the time resolution of the derived age model. This will improve the interpretation of the climate proxies extracted from this firn core and may serve as a role model for other shallow firn cores from the East Antarctic Plateau.

DOĞU ANTARKTİKA PLATOSU'NDAN ALINAN FIRN KAROTUNUN TARİHLENDİRİLMESİ VE YORUMLANMASI

ÖZET

Doğu Antarktika Platosu'ndaki yıllık ortalama sıcaklık ve birikim oranındaki potansiyel değişikliklerin tespit edilmesi ve bu değişiklikleri anlaşılması, Antarktika buz tabakasının küresel ısınmaya karşı hassasiyetinin ve gelecekteki tepkilerinin değerlendirilmesi açısından önemlidir. Buzullar ve buz tabakaları, kar birikiminin buharlaşma ve/veya erime yoluyla meydana gelen kayıplardan daha fazla olduğu durumlarda büyüme gösterir. Kutup buz tabakalarında yağan kar erimez, bunun yerine onlarca yıl boyunca yeni kar katmanlarının altında gömülür ve daha derinlere indikçe yoğunluğu artar. Ancak, Doğu Antarktika Platosu gibi çok düşük birikim oranlarına ve bu oranın mekansal değişkenliği nedeniyle, yüzyıllık ve on yıllık zaman çözünürlüğüne sahip firn karotlarından iklim göstergelerinin yorumlanması oldukça zorlayıcıdır.

Doğu Antarktika Platosu'ndaki buz karotlarının tarihlendirilmesindeki karşılaşılan temel zorluklar, bölgenin çok düşük birikim oranları ve düzensiz kar birikimi ile ilişkilidir. Düşük birikim oranları, yıllık katmanların ayırt edilmesini zorlaştırarak, geleneksel tarihleme yöntemlerinin, özellikle yıllık katman sayımı gibi tekniklerin güvenilirliğini sınırlamaktadır. Buna ek olarak, Doğu Antarktika Platosu'nda eğimlerde meydana gelen küçük değişiklikler, rüzgar yönü ve hızını etkileyerek kar birikiminde önemli değişikliklere neden olabilmektedir. Bu bölgedeki doğrudan veya dolaylı kayıtların azlığı, geçmiş buz birikim oranlarını güvenilir bir şekilde belirlemeyi güçleştirmektedir. Mevcut tarihleme yöntemleriyle elde edilebilen yaş tahminlerinin sınırlı olması ve bu yöntemlerle sağlanan belirsizlik değerlendirmelerinin düşük güvenilirliği, bu tür çalışmların önündeki en büyük engellerden biridir.

Bu çalışmada, Coldest Firn Projesi kapsamında, 16-18 Ocak 2017 tarihlerinde Doğu Antarktika Platosu'nda, deniz seviyesinden 3544 metre yükseklikte bulunan 79°19'55"G, 34°57'53"D koordinatlarında alınan 204 metre uzunluğundaki B56 firn karotu analiz edilmiştir. Sahada yapılan ölçümler sırasında, bu firn karotunun 10 metre derinliğinde gerçekleştirilen sıcaklık ölçümü yaklaşık -55.1 °C olarak kaydedilmiştir. Ayrıca, B56 firn karotunun yüzeyine yakın olan ilk bir metre kalınlığındaki kar örneklerinin ortalama yoğunluğu, dört farklı 1 metrelik örnek üzerinden hesaplanmış ve ortalama 351 kg m^{-3} olarak belirlenmiştir.

Yoğunluk verileri, her biri 113 metre derinliğe kadar birer metrelik bölümlere karşılık gelen torba ortalama yoğunluk değerleri olarak elde edilmiştir. Karotun tüm uzunluğu boyunca dielektrik profil ölçümleri yapılmıştır. Karotun ilk 70 metresi, Sürekli Akış Analizi yöntemi ile analiz edilmiş ve erimiş sudan yarı-ayrık örnekler toplanmıştır. Bu örnekler iyon konsantrasyonları açısından analiz edilmiştir.

Bu çalışmanın temel amacı, Doğu Antarktika firn karotlarının kronolojik analizi için özel olarak bir Python tabanlı tarihleme aracı geliştirmeyi amaçlamaktadır. Araştırma, Doğu Antarktika Platosundan çıkarılan 204 metre uzunluğundaki B56 firn karotunun

kapsamlı bir analizi yoluyla bu metodolojik çerçevenin uygulanmasını ve iyileştirilmesini hedeflemektedir. Çalışmanın başlıca hedefleri arasında, B56 firn karotu için en iyi zaman çözünürlüğüne sahip doğru bir derinlik-yaş ölçeği oluşturmak ve nicel birikim oranlarını belirlemek yer almaktadır. Bu amaçla, bilinen volkanik patlamalara karşılık gelen volkanik kül tabakaları gibi mutlak yaş belirteçlerinin tanımlanması ve bu belirteçlerin kronolojik çerçeveye bağlanması, mevcut yoğunluk verilerine dayalı olarak Herron-Langway yoğunlaşma modelinin kullanılması, derinlik-yaş ilişkisinin oluşturulması ve bu modelin Doğu Antarktika bağlamındaki uygulanabilirliğinin değerlendirilmesi, ve daha önce tarihlendirilmiş karotlardan elde edilen yaş ölçeklerinin, yüksek çözünürlüklü ölçümler (örneğin, dielektrik iletkenlik ve iyon kromatografisi - deniz tuzu olmayan sülfat konsantrasyonu) kullanılarak B56 karotuna uygulanması hedeflenmektedir.

İlk olarak, belirli tarihlerinin kesin olarak bilindiği varsayılarak 1815 Tambora volkanik patlaması ve Tambora volkanik olayıyla yakınlığı nedeniyle 1809 "Bilinmeyen" volkanik patlama, 1453 Kuwae volkanik patlaması, 1257 Samalas volkanik patlaması ve gözlemlenen kül tabakası (M.Ö. 1612) mutlak yaş belirteçleri olarak kullanılmıştır. Bu belirteçler, derinlik-yaş ilişkisini belirlemek amacıyla zaman serileri oluşturmada kullanılmıştır. Bu veriler ışığında, 2016-1815 CE arasında yıllık birikim oranı 0.0231 m w.e. $yıl^{-1}$ olarak, 1815-1809 CE arasında 0.0083 m w.e. $yıl^{-1}$, 1809-1453 CE arasında 0.0227 m w.e. $yıl^{-1}$, 1453-1257 CE arasında 0.0259 m w.e. $yıl^{-1}$ ve 1257 CE ile M.Ö. 1612 arasında 0.0251 m w.e. $yıl^{-1}$ olarak hesaplanmıştır. Genel ortalama birikim hızı ise 0,0247 m w.e. $yıl^{-1}$'dir. Bu mutlak yaş belirteçleri kullanılarak, 200 metre derinlikteki yaş yaklaşık 6000 yıl olarak hesaplanmıştır.

İkinci olarak, yoğunluğu verilerini değerlendirmek amacıyla derinlik-yaş ilişkisinin belirlenmesinde Herron-Langway modeli kullanılmıştır. Bu modelde, sıcaklık ve kar birikimi sabit kabul edildiği ve kar yoğunluğu ile kar yüzeyinin altındaki derinlik arasındaki ilişkinin zamanla değişmediği varsayımına dayanmaktadır. Bu yaklaşım, pratik ve hızlı bir tarihleme sürecini kolaylaştırmasına rağmen, buzul sistemlerinin zaman içinde sergilediği karmaşık dinamikleri göz ardı etmektedir. Bu yaklaşım, özellikle daha derin buz katmanları için belirsizlikleri artırma eğilimindedir. Ayrıca, sabit birikim oranlarının kullanılması, buzulun yıllık birikim eğilimleri hakkında doğrudan bilgi sağlamamaktadır. Herron-Langway modeli, torba ortalama yoğunluk verilerine en iyi uyumu 0,024 m w.e. $yıl^{-1}$ oranında bulmuş ve bu değer için %10'luk bir tolerans aralığı ±0,002 m w.e. $yıl^{-1}$'lik bir optimum birikim oranı belirlenmiştir. Kullanılan birikim oranına bağlı olarak, 200 metre derinlikte elde edilen yaş 6000 ile 7200 yıl arasında değişmektedir.

Üçüncü olarak, dielektrik profili ve deniz tuzu olmayan sülfat ($nssSO_4^{2-}$) konsantrasyon verileri, geçmişte kaydedilmiş bilinen volkanik patlamalarla eşleştirilerek başka bir derinlik-yaş modeli oluşturulmuştur. Bu yöntem daha yüksek çözünürlüklü veriler sağlamasına karşın, volkanik olayların zaman içerisinde doğru şekilde eşleştirilmesinin zorluğu, özellikle daha büyük derinliklerde belirsizliğin artmasına neden olur. Bu yöntemle, karotun ilk 70 metresi için $nssSO_4^{2-}$ kullanılarak 17 volkanik patlama ile, 70 metreden karotun tabanına kadar ise dielektrik profili kullanılarak 7 volkanik olay ile eşleştirilmiştir. Elde edilen ortalama birikim oranı 0,0254 m w.e. $yıl^{-1}$ olarak hesaplanmıştır. Bu modele göre, 200 metre derinlikteki yaş yaklaşık 6200 yıl olarak belirlenmiştir.

Doğu Antarktika Platosu'ndan alınan diğer firn karotları için yayınlanmış yaş modelleriyle kıyaslandığında, elde edilen sonuçlar iyi bir uyum göstermektedir.

Karşılaştırmalı olarak, karotun üst 40 metreye kadar olan tüm yaş modellerinin (yaklaşık olarak 1000 yıl) tutarlı olduğu, ancak Herron-Langway modelinin daha derinlerde yaşı olduğundan fazla tahmin ettiğini gözlemlenmiştir. Bu bulgular, geçmişteki birikim oranlarındaki değişikliklere işaret ettiğini ve Herron-Langway modelinde (sabit bir birikim oranı kullanarak) sapmaya yol açtığını öne sürülmektedir.

Sonuç olarak, tarihleme yöntemlerinin birleştirilmesiyle, firn karotunun tamamı için makul bir tarihleme sağlanmış ve aynı zamanda elde edilen yaş modelinin zaman çözünürlüğünü de iyileştirilmiştir. Bu çalışma, firn karotunun iklim göstergelerinin yorumlanmasını geliştirecek ve Doğu Antarktika Platosundan diğer firn karotları için bir rol modeli olarak hizmet edecektir.

1. INTRODUCTION

1.1 The Geological Evolution of the Antarctic Continent

Antarctica was once part of the ancient supercontinent known as Gondwana (Storey and Granot, 2021). This large landmass, centered on present-day Antarctica (Jokat et al., 2003), included South America, Africa, Arabia, Madagascar, India, Australia, New Zealand, and other regions (Lottes and Rowley, 1990). Around 180 million years ago (Mya), during the Jurassic period, Gondwana began to break apart because of tectonic activity (Hawkesworth et al., 1999; Veevers, 2004). As a result of Gondwana's separation, extension and crustal thinning occurred between Australia and East Antarctica, as well as between New Zealand and West Antarctica (Boger, 2011). The connection between the Antarctic Peninsula and Africa also ended (Dalziel and Elliot, 1982), causing Antarctica to drift to its current position at the South Pole (Boger, 2011).

1.2 Ice Sheets

The term "Ice Sheet" refers to massive ice bodies covering land areas greater than 50,000 km2, in contrast to "glaciers", which denote smaller ice bodies (Barry and Gan, 2011; Elias, 2021; Graham, 2011; Greve and Blatter, 2009). These large ice bodies, known as ice sheets, form through the ongoing accumulation of snow, which does not melt and gradually transforms into ice due to the overlying pressure of new snow layers (DeBeer et al., 2020; Fowler, 2003; Hambrey and Glasser, 2005; Otosaka et al., 2023). The transformation from snow to ice, known as densification, is explained in more detail in the chapter "1.5.4 Firn densification model".

Ice is a ductile material, causing the huge ice bodies to gravitationally flow towards the margins of the ice sheet, sometimes into the ocean (Thomas, 1979), where they form so-called ice shelves or ice tongues (floating) (Rignot et al., 2011; Vaughan and Doake, 1996). The interplay between the accumulation on top (i.e., the gain of mass)

and the loss of ice through calving, melting, and sublimation (i.e., mass loss) is called mass balance (Hanna et al., 2013).

During the Pleistocene epoch (2.58 million to 11,700 years ago), ice sheets in the northern and southern polar regions covered most of the Earth's surface (Barry and Gan, 2012). The Southern Hemisphere was covered by the Antarctic Ice Sheet, which extended into the Southern Ocean, and significant glaciation occurred in Patagonia. In the Northern Hemisphere, ice sheets covered major parts of North America, Europe, and northern Russia, with sea ice in the Arctic Ocean. Glaciation also affected the mountains of East Africa and Asia, including the Tibetan Plateau (Ehlers and Gibbard, 2007).

With the onset of the Holocene approximately 11,700 years ago, marking the end of the last ice age, these extensive ice sheets began to recede due to rising global temperatures (Otosaka et al., 2023). The remnants of these wide ice sheets form today's large ice sheets in Greenland and Antarctica.

1.3 The Antarctic Ice Sheet and its Formation

The geological separation process led to the opening of key oceanic passages around Antarctica, such as the Drake Passage, which was instrumental in establishing the Antarctic Circumpolar Current (ACC) (Barrett, 2003). Changes in the Southern Ocean's gates affected the circulation of sea currents (Houben et al., 2019). Hot subtropical ocean currents were directed farther from Antarctica which caused cooler waters to arrive in Antarctica (Houben et al., 2019). Simultaneously, the dropping of the concentration of carbon dioxide (CO_2) under the threshold in the atmosphere (Barrett, 2008), accelerated Antarctica's ice sheet to form and expand 34 Mya (Barrett, 2003; Bijl et al., 2013; Francis et al., 2008; Houben et al., 2019; Sun et al., 2009). This ice sheet was generally concentrated in high-altitude regions and areas dominated by low surface temperatures (Sun et al., 2009).

Antarctica reached its current position at approximately 25 Mya and is now an isolated great land mass positioned at the earth’s south pole (Pinti, 2011; Stump and Fairbridge, 2006). It is completely surrounded by the Southern Ocean (Aronson et al., 2011; Otosaka et al., 2023). Beneath the Antarctic ice sheets only 1-2% of the total land surface is exposed (Budd et al., 1987; Pinti, 2015; Stump and Fairbridge, 2006). The

total surface area spans 14,000,000 km^2 (Budd et al., 1987; Elias, 2021; Faure and Mensing, 2010; Graham, 2011; Pinti, 2015). However, Antarctica is distinct with its existing climate, low temperatures, and limited snowfall (Pinti, 2015; Van Der Veen, 1987). Should this ice mass ever completely melt, global sea levels are projected to rise by approximately 57.2 m (Siegert et al., 2022; Stump and Fairbridge, 2006).

The physiography of Antarctica is divided into two main parts separated by the Transantarctic Mountains; it bisects the continent into two primary ice sheets known as the West Antarctic Ice Sheet (WAIS) and East Antarctic Ice Sheet (EAIS) (Otosaka et al., 2023; Siegert et al., 2022).

The WAIS is located west of the Transantarctic Mountains (Oppenheimer, 1998) and is an ice sheet including approximately 3,800,000 km^3 of ice under the sea level (Joughin and Alley, 2011; Oppenheimer, 1998; Scherer, 1991). The WAIS's topography deepens inland, maintaining the integrity of the ice sheet (Joughin and Alley, 2011). Part of the WAIS emerges above sea level, forming ice shelves (Oppenheimer, 1998; Scherer, 1991). These ice shelves limit the seawater contact with the WAIS's subsurface and provide an ice sheet to stay in place and prevent it from moving. This way it works as a barrier while also protecting the sheet from melting (Joughin and Alley, 2011).

The Ross Ice Shelf is the largest ice shelf in Antarctica with a surface area of 497,000 km^2, Filchner-Ronne Ice Shelf is the second largest with a surface area of 430,000 km^2 (Siegert et al., 2022). If these ice shelves were to melt completely it is expected that the continental ice sheet would loosen and successively surge (Thomas et al., 2017). However the ocean and atmosphere are very delicate towards warming (Joughin and Alley, 2011).

Moreover, the sub-sea level positioning makes the WAIS particularly susceptible to the impact of warming ocean currents (Rignot et al., 2014). These currents erode the ice sheet from below, accelerating its melting process (Shepherd et al., 2018). A key factor in this vulnerability is the grounding line, where the ice transitions from being anchored to the bedrock to floating on the ocean (Joughin et al., 2014). Warm ocean water intrusions, as observed in the Thwaites Glacier, increase the ice sheet's instability (Scambos et al., 2017). Such changes in the WAIS represent significant

tipping points in the global climate system (DeConto and Pollard, 2016; Joughin et al., 2014).

The WAIS is losing mass and is presently the area with Antarctica's biggest impact on rising global sea levels (Naughten et al., 2023). If the WAIS were to melt completely, global sea levels are projected to rise by approximately 5 ±1 m (Bindschadler et al., 1998; Naughten et al., 2023; Oppenheimer, 1998).

The Antarctic Peninsula Ice Sheet (APIS) is situated in West Antarctica and covers the Antarctic Peninsula (Siegert et al., 2022). The peninsula's topography forms a narrow band extending from north to south. It is composed of a narrow strip of continental crust, with elevations descending from approximately 2,500 m to 1,000 m moving northward (Smellie et al., 2009). This region averages 70 km in width and a mean height of 1,500 m (Davies et al., 2012). It is considered the northernmost region of Antarctica and is characterized by a more temperate climate, which is why it is often separated from the WAIS (Otosaka et al., 2023). It has higher temperature increases compared to other regions in Antarctica (Davies et al., 2012; Otosaka et al., 2023) and covers a surface area of approximately 521,900 km^2 (Davies et al., 2012; Smellie et al., 2009). In comparison to other Antarctic ice sheets, such as the WAIS and the EAIS, the APIS shares greater similarities with the subpolar glacial systems found in coastal regions of Greenland, Svalbard, Patagonia, and Alaska (Vaughan, 2006).

The EAIS is located on the eastern side of the Transantarctic Mountains and this ice sheet makes up approximately 85% of the Antarctic ice volume (Otosaka et al., 2023). This makes it the largest continental ice mass on Earth (Mackintosh et al., 2014). The EAIS is situated at a very high elevation above sea level (Otosaka et al., 2023; Waddington and Lingle, 2013), with the ice sheet averaging around 3,000 m above sea level (Stokes et al., 2022). Despite the uneven bedrock beneath, the ice-covered surface of the East Antarctic Plateau (EAP) presents a relatively smooth and gradual slope of less than 0.5 m km^{-1}, often described as flat or undulating (González et al., 2021).

As one moves away from the coastal areas, the gradient decreases, leading to higher terrains and more extreme climatic conditions (González et al., 2021). The highest point in this region is Dome Argus (Dome A) (Ding et al., 2016), which reaches surface elevation of over 4,000 m (Waddington and Lingle, 2013; Wang et al., 2012) and records the lowest annual average temperature of -58.3 °C (Cui et al., 2009; Xiao et

al., 2008), along with an extremely low snow accumulation rate of approximately 0.020 meter water equivalent per year (m w.e. $year^{-1}$) (Cui et al., 2009). Similarly, Dome Fuji (Dome F), with an elevation of 3,800 m (Motoyama, 2007), experiences an annual average temperature of -56.5 °C (Dittmann et al., 2016; Hondoh et al., 2002; Saruya et al., 2022) and an annual accumulation rate of approximately 0.027 ±0.002 m w.e $year^{-1}$ (Dittmann et al., 2016; Saruya et al., 2022).

These conditions classify the EAIS is a polar desert, considered the driest desert in the world, with annual precipitation amounting to less than 0.1 m (Waddington and Lingle, 2013). Its climate is extremely harsh (Waddington and Lingle, 2013) and is recognized as the coldest place on the planet (González et al., 2021; Scambos et al., 2018; Turner et al., 2009). It contains the vast majority of the world's glacial ice, and if the EAIS were to melt completely, it would result in a sea level rise of approximately 52 m (Stokes et al., 2022; Zhai et al., 2024).

1.4 Ice Core as Climate Archive

The polar regions and high mountain summits are key sites for ice core collection, providing essential archives for understanding Earth's past climatic records (Thompson, 2000). When snow falls on polar ice sheets, it entraps atmospheric dust, volcanic ash, and other particles (Gabrielli and Vallelonga, 2015), including insoluble silicate matter (tephra) and gases injected into various levels of the atmosphere by volcanic eruptions (Zielinski, 2000), which then settle on the surface (Gabrielli and Vallelonga, 2015). Over time, these layers of snow accumulate, compress, and through firn formation, followed by sintering and recrystallization, transform into solid ice (Herron and Langway, 1980). This transformation process induces variations in ice density and structure, which are recorded as seasonal fluctuations in the ice core layers (Alley, 1988). Such variations are essential for deriving insights into past climate conditions (Bohleber et al., 2021). Furthermore, the air bubbles trapped within these ice cores preserve the chemical composition of the past atmosphere (Petit and Raynaud, 2020), particularly the concentrations of greenhouse gases (i.e., carbon dioxide (CO_2) and methane (CH_4)). The stable water isotope analysis, through detailed examination of the water molecules (stable oxygen isotope ratios ($\delta^{18}O$) and stable hydrogen isotope ratios (δD)) in these cores, holds information on past temperature changes and precipitation regimes (Jouzel et al., 2007).

1.5 Ice Core Dating Methods

Ice core dating is a crucial aspect of paleoclimatology, transforming raw data from ice cores into a chronological framework (Dansgaard et al., 1982). Without an accurate age scale, the valuable information on temperature variations, atmospheric dust flux, and sea ice cover retrieved from ice cores cannot be effectively used to reconstruct past climates (Alley et al., 1997).

Ice cores from East Antarctica provide valuable information on past climate variations (Masson-Delmotte et al., 2005). Different proxies account for the reconstruction of temperature variations, atmospheric flux of dust, and sea ice cover and these are measured from ice cores using standard protocols (Wolff et al., 2010). However, the information on these proxies along the ice core - i.e., with depth - is of little use unless it is transformed into an age scale (Alley et al., 1997). This transformation is achieved by dating the ice core, i.e., assigning an age to specific depths or intervals (Dansgaard et al., 1982).

Dating ice cores requires a profound knowledge of the time evolution of proxies and their uncertainties (Parrenin et al., 2007). Different tools have been developed in the past to date ice cores, utilizing absolute age markers such as volcanoes, annual layer counting using the known seasonal variations of proxies, and ice flow models (Sigl et al., 2015). These approaches are based on the fundamental assumption that snow is deposited regularly, i.e., constant over time (Fisher et al., 1985). Both the continuity of snowfall and its amount determine the possibility and quality of the age estimates (Grootes et al., 1993).

1.5.1 Absolute age markers

Absolute age markers are observations in ice cores that can be assigned to an absolute (well-known) age (Sigl et al., 2015). These markers are essential for creating accurate chronologies in ice core studies because they allow specific depths in the ice core to be correlated with precise points in time (Alley et al., 1997). Several proxies can serve as absolute age markers:

Ash Layer Volcanic ash layers, also known as tephra layers, in ice cores serve as absolute age markers for chronological dating (Lowe, 2011). These layers, resulting from volcanic eruptions, provide a method to date ice accurately (Zielinski, 2000).

Their distinct geochemical signatures enable correlation with known volcanic events (Bénédicte et al., 2010). This characteristic allows for precise cross-correlation between different ice core records, enhancing the reliability of chronological frameworks (Svensson et al., 20015).

Counting layers by stratigraphy Stratigraphic analysis of glacier layers is a fundamental method in geochronology and is based on the visual or instrumental identification of seasonal layers (Alley et al., 1997). This approach is particularly effective for recent periods, such as the Holocene (Walker et al., 2012). However, the interpretation becomes more challenging for older periods due to the disturbances in layers caused by glacial movements and other factors (Alley, et al., 1997).

Summer layers usually contain higher melt rates and more impurities, such as dust and pollen (Mayewski et al., 1994). This increase in impurities during the summer is due to higher temperatures that cause more surface melting (Mayewski et al., 1993) and the presence of stronger winds that transport dust and pollen into the ice (Fischer et al., 2007). In contrast, winter layers have fewer impurities and are typically clearer and less dense (Paterson, 1994). These seasonal variations help distinguish stratigraphic layers, facilitating accurate chronological dating (Alley et al., 1997; Paterson, 1994).

Melt layers in ice cores form due to surface ice melting during warmer periods and subsequent refreezing (Herron et al., 1981). These layers indicate past temperature fluctuations and provide data for reconstructing historical climate variations (Koerner, 1997). The characteristics of melt layers help interpret past warm seasons and climatic changes (Fisher et al., 1985).

1.5.2 Annual layer counting

Annual layer counting is based on the observation that several proxies undergo a seasonal cycle in the atmosphere, which is then reflected in their deposited concentration in the snow and ice on the ice sheet (Dansgaard et al., 1982). This seasonality can originate from the dependence on field temperature, as well as sea ice conditions, atmospheric variations, wind, and other environmental factors (Thompson et al., 2000). This method allows for a high-resolution chronological framework essential for accurately interpreting past climate data (Jouzel et al., 2007).

Stable Water Isotopes The analysis of stable water isotope ratios ($\delta^{18}O$ and δD), reflects seasonal temperature and moisture source changes, as explained by Rayleigh

fractionation processes (Jouzel and Merlivat, 1984). Isotope ratios are often reported relative to Standard Mean Ocean Water (SMOW), providing a consistent reference point for measurements.

In summer, and similarly during interglacial periods, higher temperatures increase the rate of evaporation, which leads to a higher proportion of the heavier isotope, Oxygen-18 (^{18}O), in atmospheric moisture. This process results in an enrichment of ^{18}O in the precipitation and, consequently, in ice core records, producing more positive values (Merlivat and Jouzel, 1979). Conversely, in winter, and during glacial periods, cooler temperatures and reduced evaporation lead to the relative depletion of ^{18}O in precipitation. During these colder periods, the lighter isotope, Oxygen-16 (^{16}O), becomes more prevalent in atmospheric moisture and is subsequently more dominant in ice core records, indicating cooler periods (Cuffey and Vimeux, 2001). Therefore, in ice cores, a higher prevalence of ^{18}O typically indicates warmer periods, while higher levels of ^{16}O suggest cooler periods. These isotopic variations are measured relative to the SMOW, providing a standardized comparison (Craig, 1961).

For hydrogen isotopes, the relationship can be similarly expressed using ^{1}H (or Protium) and ^{2}H (or Deuterium). Deuterium (D) is the heavier isotope of hydrogen, while Protium (H) is the lighter isotope. The isotopic fractionation for hydrogen isotopes follows a similar principle as oxygen isotopes. In summer, the higher temperatures increase the evaporation rate, leading to a higher proportion of the lighter isotope, H, in atmospheric moisture (Dansgaard et al., 1969). During winter, the heavier isotope, D, becomes more dominant in precipitation due to preferential condensation (Johnsen et al., 1972). Similar to oxygen isotopes, these hydrogen isotope ratios are also reported relative to SMOW (Craig, 1961), as shown in equations 1.1 and 1.2.

This isotopic separation process, governed by Rayleigh fractionation, results in distinct seasonal isotopic signatures within ice cores:

$$\delta^{18}O = \left(\frac{\left({}^{18}O/_{16}O \right)_{sample}}{\left({}^{18}O/_{16}O \right)_{SMOW}} - 1 \right) \times 100 \qquad (1.1)$$

$$\delta D = \left(\frac{\left({}^{D}/_{H}\right)_{sample}}{\left({}^{D}/_{H}\right)_{SMOW}} - 1 \right) \times 100 \qquad (1.2)$$

These isotopic records provide insights into historical temperature and humidity variations, enabling the reconstruction of past climatic conditions with high accuracy (Johnsen et al., 1972).

Trace Components The concentrations of trace components such as sulfate (SO_4^{2-}) and nitrate (NO^{3-}) in ice cores, influenced by environmental factors including atmospheric conditions and volcanic activities, are key indicators of past environmental conditions (Hammer et al., 1980; Zielinski et al., 1994; Delmas, 1992).

Increases in SO_4^{2-} concentrations, particularly following volcanic eruptions, result from sulfates being deposited in snow layers. These deposits form distinct stratigraphic layers in the ice cores, serving as important markers for analyzing and dating past volcanic events (Zielinski et al., 1994). NO^{3-} concentrations, on the other hand, are influenced by sources such as lightning, soil emissions, biomass burning, and fossil fuel combustion. Variations in NO^{3-} levels can provide insights into changes in atmospheric chemistry and human impact on the environment over time (Legrand and Mayewski, 1997).

1.5.3 Ice flow modeling

Ice flow modeling is a method in glaciology for understanding the dynamics of ice sheets and glaciers. These models simulate the movement and deformation of ice, enabling the inference of the origin and age of ice layers based on current ice sheet characteristics, such as accumulation rates, flow velocities, and topography (Paterson, 1994).

Ice flow models typically consist of several key components: a mechanical model describing the deformation and flow of ice, an accumulation model for historical snowfall rates, age markers within the ice core, and inverse methods to refine model parameters (Huybrechts, 1994). These models not only provide age estimates but also enable the reconstruction of past accumulation rates and surface elevations, thus offering insights into historical climatic conditions (Parrenin et al., 2007).

Furthermore, these models can simulate the impacts of climate change on ice dynamics, predicting future changes in ice sheet behavior and their contributions to

sea level rise. By incorporating various physical processes and environmental data, ice flow models serve as essential tools for both reconstructing past ice dynamics and forecasting future changes (Ritz et al., 2001).

1.6 Firn densification model

Glaciers and ice sheets grow when the accumulation of snow is greater than the loss due to sublimation and/or melt. At the polar ice sheets, the deposited snow does not melt. It gets buried under new layers of snow over decades, becoming denser as it goes deeper. This transformation from snow to ice is called firn densification (Freitag et al., 2004; Hörhold et al., 2011; Hörhold et al., 2012).

Several models have been developed to represent the process of firn densification. These models use variables such as the rate of snow accumulation, annual mean temperature, heat conduction, etc. to express the increasing density with depth under different local climate conditions (Arnaud et al., 2000; Barnola et al., 1991; Goujon et al., 2003; Herron and Langway, 1980).

1.7 Motivation

For East Antarctic firn cores, the very low accumulation as well as intermittent deposition hamper and challenge dating approaches. Most of the time, only volcanic eruptions allow for single time stamps along the ice core. There are only limited possibilities and approaches to derive an age scale between volcanic eruptions. This also implies that it is impossible to derive any variations in climate (i.e., proxies) on smaller than millennial to centennial time scales.

Given these challenges, adopting approaches to date firn cores using available data from common measurements like density, dielectric profiling, or ion chromatography becomes essential. Improving the dating of these cores is crucial for analyzing climate variations in the past few millennia. Advancements in these dating techniques are fundamental for a comprehensive understanding of the implications of global warming on the Antarctic environment.

1.8 Scope of This Study

This study seeks to develop a Python-based dating toolbox specifically for the chronological analysis of East Antarctic firn cores. This research aims to apply and refine this methodological framework through a comprehensive analysis of the 204-meter-long B56 firn core extracted from the EAP. The primary objectives of this study include establishing an accurate depth-age scale for the B56 firn core with the best time resolution and determining quantitative accumulation rates. The research is structured around a series of strategic goals:

- Identification of absolute age markers, such as volcanic ash layers corresponding to known eruptions (e.g., Tambora, Kuwae, Samalas), for linking to the chronological framework.
- Utilization of the Herron-Langway densification model, based on density data, to construct a depth-age relationship and evaluate its applicability in the East Antarctic context.
- Application of existing age scales, derived from previously dated cores, to the B56 core using high-resolution measurements such as dielectrical conductivity and non-sea-salt sulfate concentration.

In conclusion, the development of a Python-based dating toolbox for analyzing East Antarctic firn cores in this study, and its application to the B56 core, is intended to advance our understanding of the East Antarctic climate history ultimately. By identifying absolute age markers, employing the Herron-Langway densification model, finding volcanic eruptions using non-sea-salt sulfate concentration, matching using dielectric profiling, and applying existing age scales, the aim is to refine a detailed chronological framework for the EAP ice depositional environment. This will aid in the paleoclimatology field when using ice cores as paleoclimate archives.

2. MATERIAL AND METHODS

2.1 Available Data and Scripts

2.1.1 Dating toolbox with Python

A toolbox for dating Greenland firn cores was developed (Krug, 2021-unpublished). This toolbox consists of a semi-automatic structure combining both automatic and manual dating methods. Depending on data availability, this toolbox can function either independently or in coordination. It has been applied to a Greenland firn core and allowed the generation of an age model. The toolbox includes several operational options: absolute age markers (e.g., events where the age/date is well known and defined), a downcore age estimate, using the the Herron-Langway densification model (HL model), a core-to-core matching of volcanic signals, and manual layer counting.

Selected methods included in the toolbox designed for dating shallow firn cores in Greenland were modified and utilized for dating East Antarctic firn cores. These methods comprise absolute age markers, the HL model, and matching using non-sea-salt sulfate ($nssSO_4^{2-}$) concentration and dielectric profiling (DEP). However, in this project, instead of directly applying the existing toolbox's Python codes, these codes were reprogrammed specifically for dating firn cores extracted from the Antarctic Plateau in East Antarctica, where accumulation rates are much lower compared to Greenland.

2.1.2 The B56 site and available measurements

Within the scope of the Coldest Firn (CoFi) project on the EAP, five firn cores were drilled in different locations on the EAP (Figure 2.1). These comprise cores B51 (15°S 75°W), and B53 (32°S 77°W) drilled in 2012-2013, and cores B54 (30°S 79°W), B55 (41°S 79°W), and B56 (35°S 79°W) drilled in 2016-2017 (Weinhart et al., 2020).

The B56 firn core was drilled between January 16-18, 2017 (Weinhart et al., 2020), approximately 249 km southwest of Dome F. This location, specified at 79°19'55"S, 34°57'53"E, is at an altitude of 3544 m above sea level. The on-site measurement of temperature at a depth of 10 m in the borehole of this firn core was recorded as

approximately -55.1 °C (personal communication with Sepp Kipfstuhl). Additionally, the initial snow density (i.e., surface density) of the upper meter of the B56 firn core, averaged over four one-meter samples, was calculated to be 351 kg m^{-3} with the variance between the four liners being 8 kg m^{-3} (Weinhart et al., 2020).

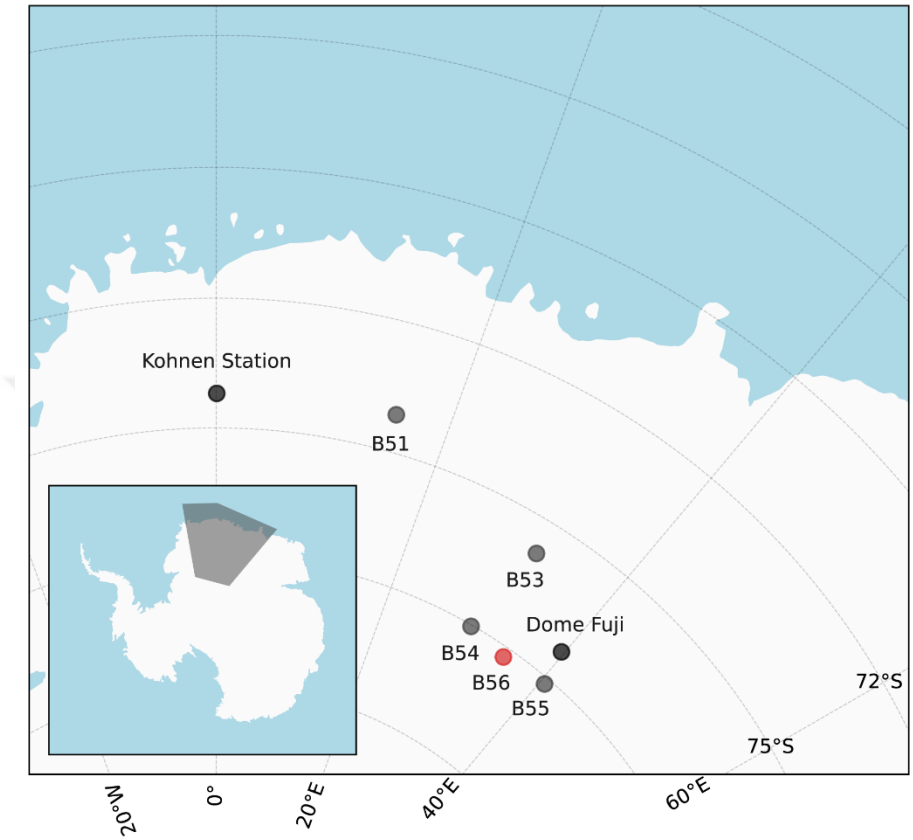

Figure 2.1 : The drilling sites within the CoFi project, namely B51, B53, B54, and B55 locations, have been marked in gray on the map. The focus of this thesis, B56 core, is highlighted in red. Dome F and Kohnen Station are indicated in black on the map. A dark grey shading in the bottom left corner represents the location in Antarctica.

The B56 firn core was drilled to a length of 204 m. Density data is provided as bag mean density values, with each corresponding to one-meter sections down to 113 m depth. Additionally, DEP was conducted on the full length of the core in the ice lab of Alfred Wegener Institute (AWI) Bremerhaven. The upper 70 m of core were analyzed applying a Continuous Flow Analysis (CFA), where semi-discrete samples were collected from the meltwater. These samples were analyzed for ion concentrations using an ICS-5000 ion chromatography system. In this project, the SO_4^{2-} concentration is used. It is measured with an accuracy of ±0.1 µg L^{-1}.

2.2 Implementation of the Dating Methods

2.2.1 Absolute age markers

To construct chronological frameworks for the B56 firn core, well-dated volcanic eruptions were used as absolute age markers. These volcanic eruptions, Tambora (Stothers, 1984), Kuwae (Gao et al., 2006; Witter and Self, 2006), and Samalas (Lavigne et al., 2013), served as reference points due to their absolute time markers. These markers were identified by analyzing nssSO_4^{2-} and DEP (of conductivity) data. In addition, the presence of a distinct ash layer in the firn core, identified using DEP, served as a chronological marker.

2.2.2 The HL model and its application for dating

In this chapter, the empirical model by Herron and Langway (1980) is introduced, and its application for age estimate is shown in the case of the B56 firn core. First, to analyze the change in density with depth, a graph of the bag mean density values corresponding to each one-meter section was created (Figure 2.2). For the remaining part of the core (from 113 m to 204 m), the estimated density values were calculated using the sigmoid interpolation method.

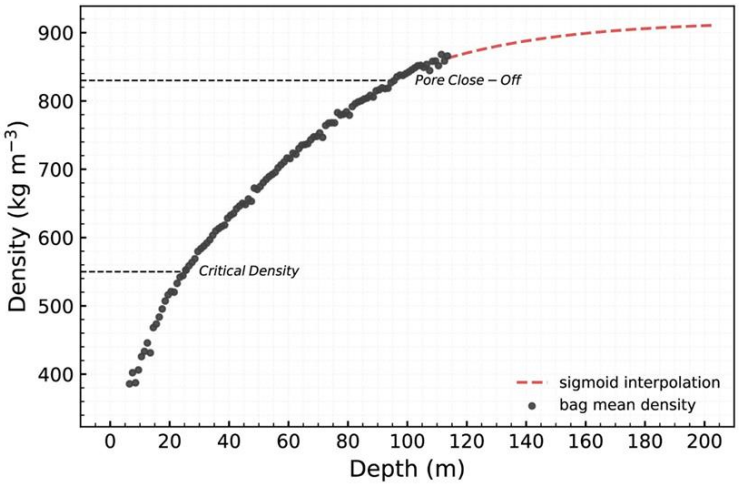

Figure 2.2 : The bag mean density of the B56 firn core, shown as black dots representing measured densities from one-meter sections, is plotted against depth. The red dashed line illustrates the estimated density data using sigmoid interpolation. Grey dashed lines indicate a critical density of 550 kg m^{-3} and a pore close-off density of 830 kg m^{-3}, corresponding to depths of 25.15 m and 95.57 m, respectively.

The HL model is a simple empirical model that has proven to work in most studies (Goujon et al., 2003; Herron and Langway, 1980; Zwally and Jun, 2002). This model is mainly driven by key factors including field temperature, the rate of snow

accumulation, and the pressure exerted by overlying snow layers. Similar to other models, the HL model categorizes firn densification into three distinct stages (Arnaud, 2000; Bertler, 2011; Freitag et al., 2004; Herron and Langway, 1980; Lundin et al., 2017; Spencer et al., 2001).

The first stage, extending from the surface to a critical density threshold of 550 kg m^{-3}, initiates with surface snow possessing a density typically ranging between 300-350 kg m^{-3}, equating to a porosity of approximately 62% to 67% (Bender et al., 1997). As new snow accumulates, the snowpack, initially lighter than 550 kg m^{-3}, undergoes compaction under the weight of the overlying layers (Bertler, 2011), transitioning into what is known as firn (Alley, 1987; Arnaud, 2000; Faria et al., 2017; Herron and Langway, 1980). This transition, marked by the initial snow density up to the critical density of 550 kg m^{-3}, is characterized by the most rapid rate of densification, involving mechanisms such as packing, grain-boundary sliding, and grain growth (Alley, 1987; Arnaud, 2000; Herron and Langway, 1980). At the point where density reaches approximately 550 kg m^{-3}, the average porosity drops to around 40% (Alley, 1987), and beyond this density, grain-boundary sliding ceases to be the dominant densification process, giving way to intercrystalline plastic deformation or creep (Arnaud, 2000).

The second stage, contained densities from the critical density of 550 kg m^{-3} to pore close-off of 820-840 kg m^{-3}, is characterized by the continued compaction and sintering of older snow under increasing overburden pressure and with increasing depth (Faria et al., 2017). This stage exhibits a slower increase in density ratio with density (Herron and Langway, 1980). During this phase, the interconnected pore network within the firn facilitates air exchange with the atmosphere above (Buizert, 2013). Eventually, at the base of the firn column, the air becomes permanently encapsulated within the ice matrix, capturing an atmospheric sample from the time of pore close-off (Buizert, 2013). Bubble formation continues until the closure of air passageways (Faria et al., 2017; Herron and Langway, 1980).

The third stage encompasses the transition from pore close-off, occurring at densities between 820-840 kg m^{-3}, to the formation of glacier ice, which is typically at a density of 917 kg m^{-3}, indicative of pure ice. Pore close-off signifies the cessation of bubble creation, with pre-existing bubbles becoming trapped and compressed as the air

passageways close (Herron and Langway, 1980). This compression marks the final phase of snowpack densification, leading to the formation of glacier ice.

As input parameters for the model, empirical values of the site-specific parameters, including the annual mean temperature, annual mean accumulation rate, and surface density (i.e., initial snow density), are used to drive the model. The values that best fit the measured bag mean density of the B56 firn core are determined for the annual mean accumulation rate.

- Initial snow density (ρ_0) = 351 kg m^{-3} (This value was obtained from Weinhart et al., 2020)
- Annual mean temperature (T) = -55.1 °C (218.05 K, personal communication with Sepp Kipfstuhl)

The model uses the following constants:

- Gas constant (R) = 8.314 J K^{-1} mol^{-1}
- Density of ice (ρ_i) = 917 kg m^{-3}
- Critical density (ρ_{550}) = 550.0 kg m^{-3}

The rate constant for densification in the first stage (k_0), represents the densification rate in regions where the density is ρ_{550} or less (Equation 2.1).

$$k_0 = 11\, e^{-\frac{10160}{R\,T}} \tag{2.1}$$

The rate constant for the densification in the second stage (k_1), determines the densification rate in regions where the density exceeds ρ_{550} (Equation 2.2).

$$k_1 = 575\, e^{-\frac{21400}{R\,T}} \tag{2.2}$$

In these equations, R is the universal gas constant, and T is the annual mean temperature in K.

Table 2.1, the rate constants indicate the relationship between T and densification rate. The densification in the first stage ($\rho \leq \rho_{550}$) and the densification in the second stage ($\rho > \rho_{550}$) of the densification processes show a trend for the reaction rates to increase with T for the rate constants. The k_1 appears to be more sensitive to T changes compared to the rate k_0.

Table 2.1 : Values of rate constants (k_0 and k_1) for specified T values

T, °C	$k_0 \times 10^{-5}$	$k_1 \times 10^{-6}$
-54	4.17	4.56
-55	4.06	4.32
-56	3.96	4.09
-57	3.86	3.87
-58	3.76	3.66
-59	3.66	3.46

The depth at which the transition from one stage to the other, related to the ρ_{550}, is mainly determined by the T (see equation 2.3). The measured T for ρ_{550} shows a trend where, as the T decreases, the depth at the critical density (h_{550}) increases.

$$h_{550} = \frac{1}{p_i k_0}\left[ln\left(\frac{\rho_{550}}{\rho_i - \rho_{550}}\right) - ln\left(\frac{\rho_0}{\rho_i - \rho_0}\right)\right] \tag{2.3}$$

This indicates that at colder temperatures, the snowpack reaches the ρ_{550} at a deeper level, suggesting that colder temperatures contribute to denser snow at greater depths within the snowpack (Table 2.2).

Table 2.2 : The depth at which the ρ_{550} is reached, as a function of different T

T values for k_0	h_{550}, m
-54 °C	23.10
-55 °C	23.70
-56 °C	24.32
-57 °C	24.96
-58 °C	25.62
-59 °C	26.31

Following the calculations for the critical density value in the dataset (ρ_{550}, h_{550}, and t_{550}, where t_{550} denotes the age of the critical density), Z_0 (which represents the density at specific depths for the first stage of densification, see equation 2.4) and the ρ_h (density values, depth profile for the first stage of densification) are determined using the rate constant k_0 for regions below this critical value. Similarly, for the stage above the ρ_{550}, Z_1 (which represents the density at specific depth for the second stage of densification, see equation 2.4) and the ρ_h (density values, depth profile for the second stage of densification) are calculated using the rate constant k_1.

$$\begin{aligned} Z_0 &= e^{\rho_i k_0 h + \ln\left(\frac{\rho_0}{\rho_i - \rho_0}\right)}, \quad \rho_h = \frac{\rho_i Z_0}{1 + Z_0} \\ Z_1 &= e^{\frac{\rho_i k_1 (h - h_{550})}{\sqrt{A}} + \ln\left(\frac{\rho_{550}}{\rho_i - \rho_{550}}\right)}, \quad \rho_h = \frac{\rho_i Z_1}{1 + Z_1} \end{aligned} \tag{2.4}$$

The depth-density profile obtained from the ρ_h formula based on the HL model has been compared with the actual depth-density data obtained from the B56 firn core. Specific parameters for the annual mean accumulation rate (A) and T have been determined to assess the harmony between these two sets. These results are detailed in the "Age Model from HL Model" section.

In order to determine t_{550}, the model was assessed using the rate constant k_0 specific to the first stage (Equation 2.5)

$$t_{550} = \frac{1}{k_0 A} \ln\left(\frac{\rho_i - \rho_0}{\rho_i - \rho_{550}}\right) \tag{2.5}$$

Accordingly, the calculated age at the ρ_{550} is determined by the T (in k_0) and the A. To assess the sensitivity of the derived age, different T and A values are used as input parameters, and the resulting ages are compared (Table 2.3).

Table 2.3 : Age of ρ_{550} at different T and A

Measured	A, m w.e. year^{-1}		
T, °C	0.010	0.020	0.030
-54 °C	976 CE	1496 CE	1669 CE
-55 °C	949 CE	1483 CE	1660 CE
-56 °C	921 CE	1469 CE	1651 CE
-57 °C	892 CE	1454 CE	1641 CE
-58 °C	862 CE	1439 CE	1631 CE
-59 °C	831 CE	1424 CE	1621 CE

Table 2.3 illustrates the effect of different T values and A on the age of ρ_{550}. Specifically, an increase in A at a certain T tends to result in a decrease in the age of ρ_{550}. This phenomenon is associated with the thickness of the snow layer. Additionally, comparisons of A at different T values indicate conditions where a decrease in T correlates with a slower rate of densification, indicating that the age of ρ_{550} increases.

The calculation of time corresponding to a specific density (t_ρ), derived from ρ_h, enables the establishment of a comprehensive depth-age profile for firn by capturing the relationship between density values and age (Equation 2.6).

$$t_\rho = \frac{1}{k_1\sqrt{A}} \ln\left(\frac{\rho_i - \rho_{550}}{\rho_i - \rho}\right) + t_{550} \tag{2.6}$$

Consequently, it facilitates the calculation of age variations associated with different density values at various depths, thereby constructing a depth-age profile. The detailed

examination of these outcomes is presented in the “Age model from HL model” section.

2.2.3 Finding volcanic eruptions using nssSO_4^{2-} data

SO_4^{2-} might be derived from sea salt and marine biogenic emissions and brought in via atmospheric transport, volcanic eruptions are the major source of SO_4^{2-} (Igarashi et al., 2011). To identify volcanic signals in the B56 firn core, a concentration profile of nssSO_4^{2-} ions has been measured. This analysis of SO_4^{2-} is utilized for differentiating between marine-derived sulfate and sulfate of volcanic origin. Given the geographical location of B56 is far from the ocean, it is likely that most sulfate found here comes from volcanic eruptions. Nevertheless, considering that atmospheric circulation and winds can transport sea salt-derived sulfate particles over long distances, this method has been employed to distinguish between volcanic and marine sulfate sources, thereby enabling the determination of volcanic-origin SO_4^{2-} accumulations in firn core.

In calculating the nssSO_4^{2-} concentration, it is considered that SO_4^{2-} ions from sea salt sources are typically found with sodium (Na+) ions (Figure 2.3). This indicates that the primary source of Na+ ions in the analyzed samples is sea salt.

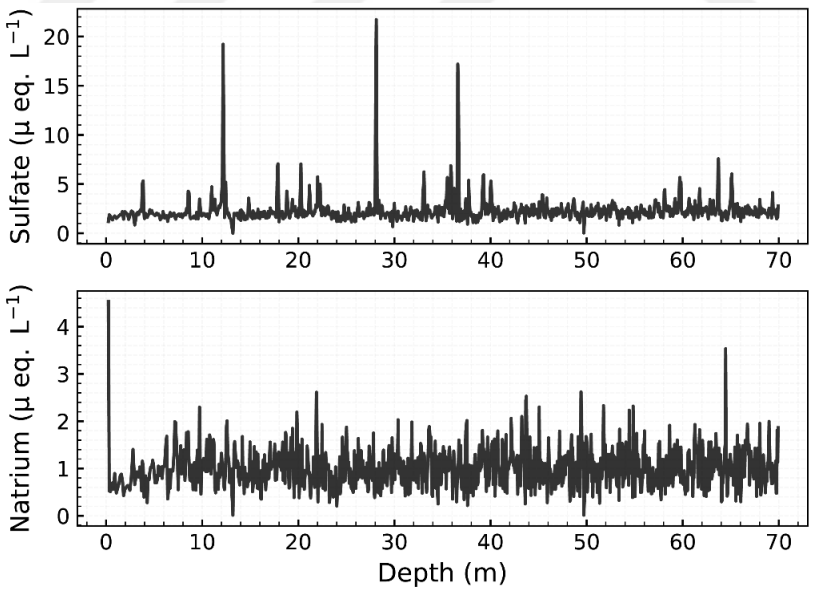

Figure 2.3 : The profiles of SO_4^{2-} and Na^+ concentrations, obtained in terms of μ eq. L^{-1}, are shown, with the top graph illustrating the concentration profile of SO_4^{2-}, and the bottom graph presenting the concentration profile of Na^+. These profiles indicate the variations in the concentrations of these ions with increasing depth in the B56 firn core.

To determine the $nssSO_4^{2-}$ concentration, the contribution of Na^+ ions is subtracted from the total SO_4^{2-} concentration, as shown in equation 2.7.

The equation used for this calculation is:

$$nssSO_4^{2-} = SO_4^{2-} - 3.02 \times 10^{-2} \times Na^+ \qquad \text{(Igarashi et al., 2011) (2.7)}$$

Here, $nssSO_4^{2-}$ represents the concentration of non-sea-salt sulfate ions and is used to identify sulfate of volcanic origin. SO_4^{2-} denotes the total sulfate ion concentration measured in the core, which includes sulfate from both sea salt and other sources. Na^+ indicates the sodium ion concentration measured in the core and, being the marine origin, serves as an indicator for calculating sea-salt-derived sulfate. The value 3.02 $\times 10^{-2}$ represents the ratio of SO_4^{2-} to Na^+ ions in seawater. This ratio is used to estimate the proportion of sulfate derived from sea salt, which is then subtracted from the total sulfate concentration to obtain the $nssSO_4^{2-}$ concentration.

Based on the calculated $nssSO_4^{2-}$ values, a depth-$nssSO_4^{2-}$ graph was created and used to identify potential signals of volcanic eruptions (Figure 2.4).

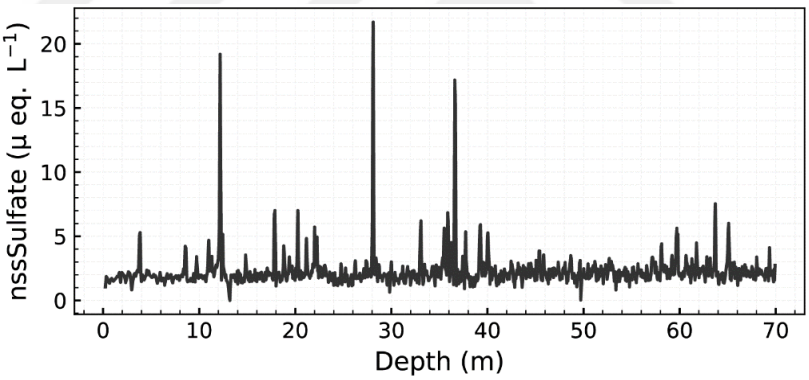

Figure 2.4 : The depth profile illustrates the variations in $nssSO_4^{2-}$ concentration with increasing depth in the B56 firn core. This profile provides information about the presence and distribution of $nssSO_4^{2-}$ ions, which originate from sources other than sea salt, throughout the core.

A threshold value was determined to predict potential volcanic eruptions using the mean (M) and standard deviation (σ) of the calculated $nssSO_4^{2-}$ values. The calculated M = 2.29 μ eq. L^{-1} and σ = 1.39 μ eq. L^{-1} represents the general distribution and average behavior of the $nssSO_4^{2-}$ dataset (Figure 2.5).

The M+2σ value was used as a threshold to identify significant peaks in the $nssSO_4^{2-}$ profile (Igarashi et al., 2011). Peaks exceeding this threshold were considered important deviations indicating volcanic signals. Initially, peaks exceeding M+2σ = 5.08 μ eq. L^{-1} were selected.

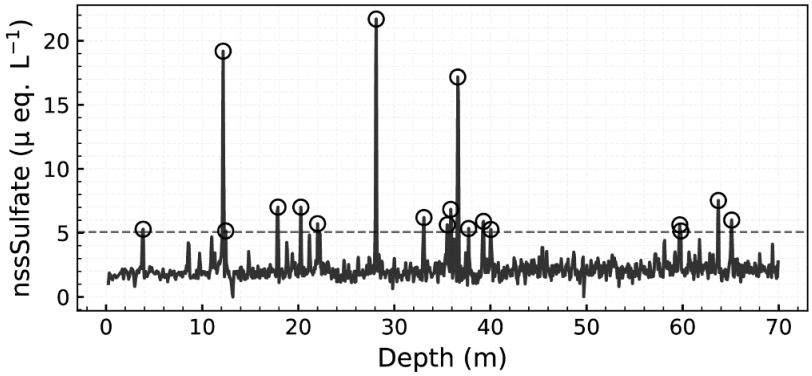

Figure 2.5 : In the $nssSO_4^{2-}$-depth profile, there are 18 peak points identified above the value (5.08 μ eq. L^{-1}) indicated by the dashed line.

Therefore, to obtain a more accurate and representative threshold, the mean after exclusion (M') and standard deviation after exclusion (σ') were recalculated. The new values were M' = 2.12 μ eq. L^{-1} and σ' = 0.63 μ eq. L^{-1}. Using these new values, peaks above M'+2σ' = 3.38 μ eq. L^{-1} were selected (Figure 2.6).

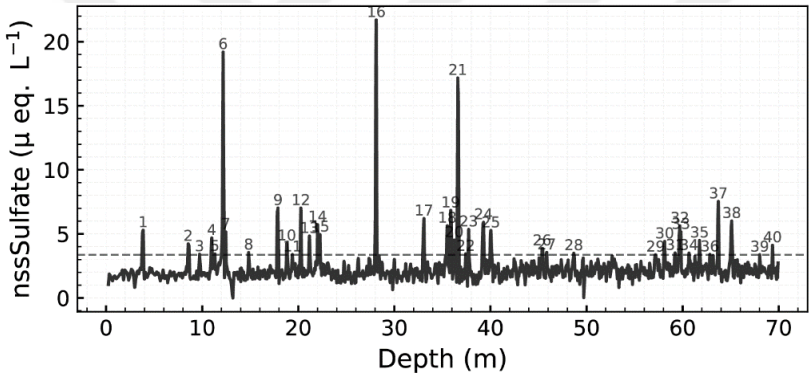

Figure 2.6 : The threshold value of 3.38 μ eq. L^{-1} is depicted as a dashed line in the graph. The 40 peaks exceeding this threshold were labeled sequentially.

Forty peaks exceeding the threshold value of 3.38 μ eq. L^{-1}, as shown in Figure 2.6, signifies potential indications of volcanic eruptions in the $nssSO_4^{2-}$-depth profile. The identification of these peaks allows for the transformation of depth- $nssSO_4^{2-}$ data into a depth-age profile.

2.2.4 Matching using DEP data

The DEP were measured along the full core, allowing an overlap and comparison with the matching from the 70 m $nssSO_4^{2-}$ profile (Figure 2.7). DEP data were used to apply matching with previously published peaks of both, $nssSO_4^{2-}$ and DEP from literature (eg. Castellano et al., 2005; Cole-Dai et al., 2000). The DEP profile provides information on conductivity variations within the ice core.

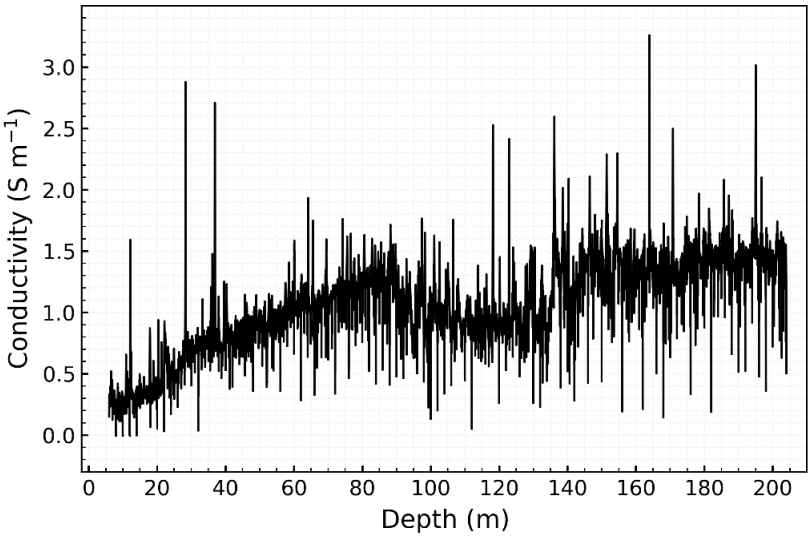

Figure 2.7 : The profile illustrates the variation in conductivity in the core, measured in S m^{-1} ×10^{-7}, with increasing depth.

As shown in Figure 2.7, the recorded conductivity measurements exhibit fluctuations with depth, reflecting changes in the physical and chemical properties of the B56 firn core. These variations are attributed to specific events, allowing the transformation of depth-conductivity data into depth-age data.

2.2.5 Conversion from snow-ice depth to water-equivalent depth

The conversion of m depth (snow-ice) to m depth (water-equivalent, w.e.) enables the normalization of data across stratigraphic layers with variable densities. The measured depths are converted into w.e. depths to yield a standardized measure. This measure reflects the equivalent volume of water that would correspond to the ice mass within each layer, considering the specific density of the firn (Figure 2.8).

The w.e. depth of an ice core, represented as $h_{w.e.,n}$ for a specific stratigraphic layer n, is determined through a calculation that integrates the physical properties of the underlying layers (Equation 2.8).

The conversion from m to meters water equivalent (m w.e.) is computed using the formula:

$$h_{w.e.,n} = h_{w.e.,(n-1)} + \left(h_{m,n} - h_{m,(n-1)}\right) \times \rho_{(n-1)} \qquad (2.8)$$

In this expression:

- $h_{w.e.,n}$ indicates the depth in m w.e. at the n-th layer, converting the depth of firn to the equivalent depth of a water column with equivalent mass.

- $h_{m,n}$ is the actual depth in m at the *n*-th layer, which directly measures the ice core's vertical extent at that layer.
- The difference ($h_{m,n}$ - $h_{m,(n-1)}$) represents the thickness of the *n*-th layer, obtained by subtracting the depth of the preceding layer, $h_{m,(n-1)}$, from the depth of the current layer.
- $\rho_{(n-1)}$ denotes the density of the firn at the (*n*-1)-th layer. This density factor, when applied to the thickness of the ice layer, provides the w.e. depth.

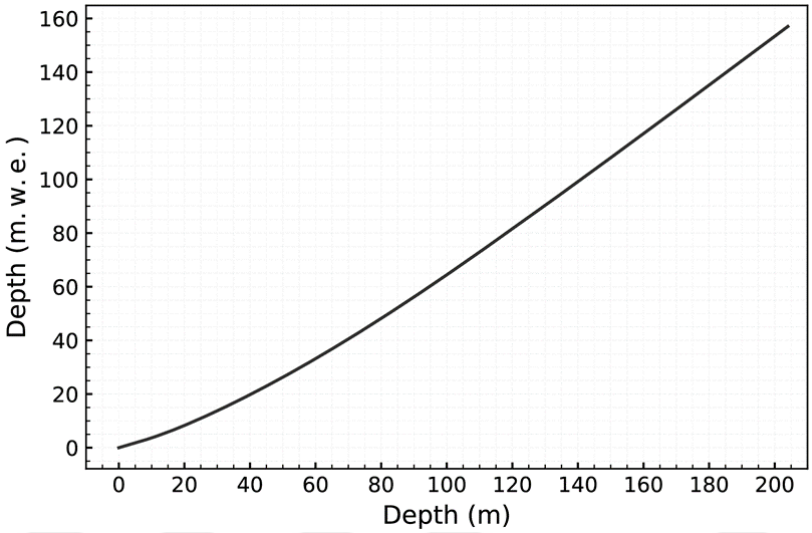

Figure 2.8 : This graph illustrates the relationship between depth of snow-ice and the corresponding depth of w.e., both expressed in m.

The formula is applied iteratively, allowing for the layer-by-layer addition to the total depth in m w.e., commencing at the surface and advancing downward through the firn core.

2.2.6 Confidence interval

To calculate the uncertainty area between depth-age values identified with volcanic eruptions, the midpoint between two values should have the maximum uncertainty because it is the farthest from both values. This uncertainty is expressed using a Z-score of approximately 1.96, corresponding to a 95% confidence interval.

The Euclidean distance (*d*) formula is used to calculate the distance between two values (Equation 2.9):

$$d = \sqrt{(x_{n+1} - x_n)^2 + (y_{n+1} - y_n)^2} \tag{2.9}$$

To calculate the confidence interval (*CI*) using the *d*, the following formula is applied (Equation 2.10):

$$Cl = \frac{U_n + U_{n+1}}{2} + c \times \frac{d}{2} \times 1.96 \qquad (2.10)$$

Here, U_n and U_{n+1} are the uncertainties identified with the two values, *c* is an adjustment factor.

These calculated uncertainty areas are used in the depth-age graph to visually represent the uncertainty between the depth-age values identified with volcanic eruptions in the B56 firn core.

3. RESULTS

In this chapter, the different age models from the three different dating approaches, absolute age markers, HL model, and matching using $nssSO_4^{2-}$ and the DEP are presented and then compared to each other.

3.1 Age Model from Absolute Age Markers

In order to test and validate the dating method by using absolute age markers, the tie points shown in Figure 3.1 are designated as absolute age markers, assuming their specific date is known for sure. Four specific data peaks P_1-P_2, P_3, and P_4 are chosen along with the ash layer (P_5) from the DEP. Additionally, the year of drilling (P_0) is indicated.

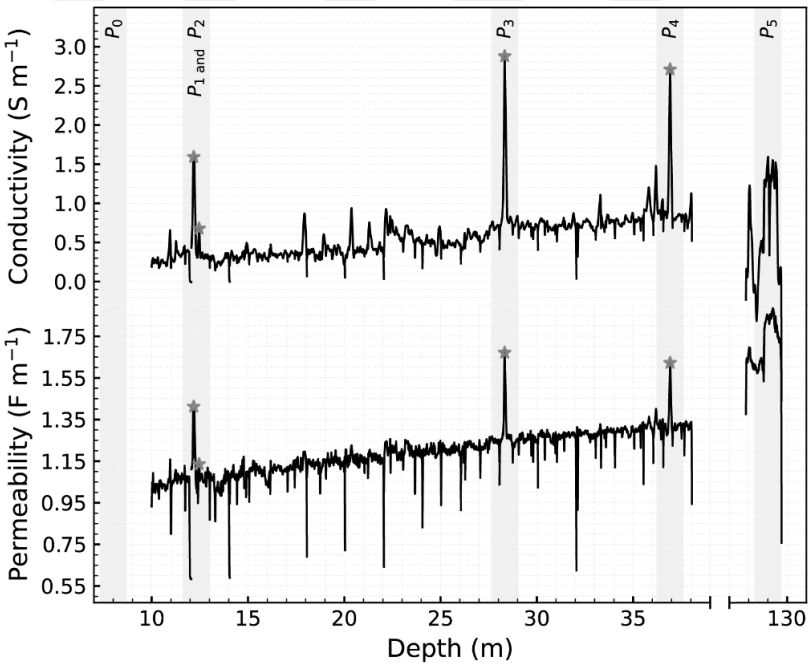

Figure 3.1 : The conductivity and permittivity measured by DEP, scaled by $\times 10^{-7}$ and $\times 10^{-13}$ respectively. P_0, P_1-P_2, P_3, P_4, and P_5 are represented and marked by gray bars.

The three peaks represent the known and well-dated volcanic eruptions of Tambora (P_1), Kuwae (P_3), and Samalas (P_4).

P_1 is commonly linked to the Tambora volcanic event primarily due to its characteristic twin peaks or closely situated dual peaks and given its proximity to the 1809 "Unknown" (P_2) volcanic event at comparable depths as seen in other firn cores (Anschütz et al., 2011; Hofstede et al., 2004; Karlöf et al., 2000; Moore et al., 1991; Oerter et al., 2000; Van Liefferinge et al., 2021). The volcanic event is interpreted to result from the Tambora volcanic eruption in the year 1815 CE (Stothers, 1984) with the chemical signature deposited in the ice in 1816 CE (Cole-Dai et al., 2009; Raible et al., 2016). The volcanic eruption of 1809 CE, occurred approximately six years before the Tambora eruption in question, with its deposition uncertainty corresponding to 1810-1811 CE (Cole-Dai et al., 2009).

On the other hand, P_3 and P_4 peaks are associated with the commonly recognized Kuwae volcanic eruption and the Samalas volcanic eruption or 1259 "Unknown" volcanic eruption (Anschütz et al., 2011; Hofstede et al., 2004; Karlöf et al., 2000; Moore et al., 1991; Oerter et al., 2000; Van Liefferinge et al., 2021). The Kuwae eruption occurred approximately in 1453 CE, with its deposition continuing until 1457 CE (Gao et al., 2006; Witter and Self, 2006). P_4 is associated with the volcanic eruption of 1257 CE Samalas and the 1259 "Unknown" volcanic eruption. Therefore, these two eruptions have been considered together. The impact of the Samalas eruption continued until approximately 1259 CE (Lavigne et al., 2013), while the "Unknown" eruption accumulated until 1261 CE (Narcisi et al., 2019). Consequently, Samalas has been designated as occurring in 1257 CE, with a deposition uncertainty of +4.

The visible ash layer (P_5), observed in the firn core at a depth of 129.3 m, is given as 1613 BCE ±5 years in the Dome Fuji 2 (DF2) core at 122.2 m, 1613 BCE ±5 years in the New Dome Fuji (NDF) core at 133.5 m, and 1612 BCE ±4 years in the New Dome Fuji North (NDFN) core at 118.7 m (Oyabu et al., 2023). Additionally, the EPICA Dome C (EDC) core at 132.6 m has dated the ash layer to 1611 BCE ±5 years (Narcisi et al., 2005). In the nearby firn cores B54 and B55 (refer to map Figure 2.1), the ash layer is seen at depths of 121.9 m and 124.9 m, respectively (Mertes, 2018 - unpublished). According to unpublished data, the age of this depth has been determined to be approximately 1612 BCE (for B54 by Joe McConnell). Assuming that the ash layer observed in all these cores originates from the same event, the ash layer in the B56 core dates to an age of 1612 BCE ±6 years.

These five absolute age markers identified in the B56 core allow for the creation of a depth-age model (Table 3.1).

Table 3.1 : Absolute age markers matched with DEP data

Volcanic eruption	Eruption year	Uncertainly, deposition year	Depth, m	Permeability, $\times 10^{-13}$ F m^{-1}	Conductivity $\times 10^{-7}$ S m^{-1}
Surface	2016 CE	-	00.0	-	-
Tambora	1815 CE	+1	12.2	1.40	1.59
Unknown	1809 CE	+2	12.5	1.14	0.68
Kuwae	1453 CE	+4	28.3	1.68	2.88
Samalas	1257 CE	+4	36.9	1.62	2.71
Ash Layer	1612 BCE	±6	129.3	-	-

The uncertainty areas, demarcated with 95% confidence intervals (see Section 2.2.6 for confidence interval calculations) between these age markers, have been recognized. These age markers, connected through the uncertainty areas, have been integrated into the model. In the model, extrapolation has been applied to the sections deeper than the oldest tie point (P_5), extending down to the core's deepest point at 204 m. In this extrapolated section, uncertainty areas have also been defined with 95% confidence intervals (Figure 3.2). This approach enables a first estimate of the age of the firn core in greater depths.

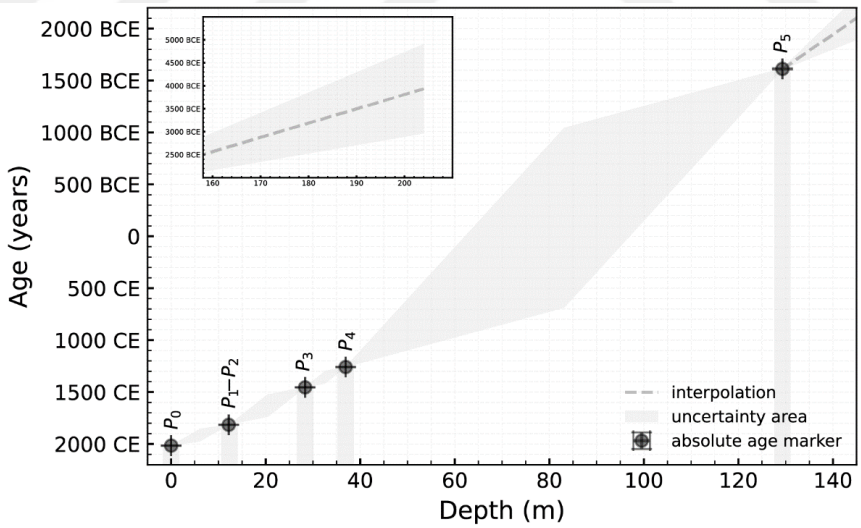

Figure 3.2 : Depth-age model from absolute age markers. The year of drilling is indicated at P_0, and the age markers P_1-P_2, P_3, P_4, and P_5 are shown with black error bars and grey bars. The dark grey dashed line indicates the extrapolation from P_5 to the final depth of the core. The areas of uncertainty are illustrated in grey.

From this age model, we can estimate the B56 core to reach back to approximately 3932 BCE ±973 years, with the deepest absolute age marker situated at 129.3 m depth with an age of approximately 1612 BCE. The uncertainty of this age model is related

to the distribution of the tie points. The uncertainty is smallest near the tie points, where the absolute age is known. The uncertainty increases as the distance between the connection points increases, and the uncertainty at the furthest distance between the connection points, that is, the exact middle point, can be as large as ±575 years (see between P_4 and P_5 is approximately 92.5 m). The closest distance between these connection points (specifically between P_3 and P_4, excluding P_1-P_2) is approximately 8.6 m, with a maximum uncertainty of ±60 years.

3.2 Age Model from HL Model

3.2.1 Sensitivity analysis and resulting age uncertainty

As the HL model is predominantly influenced by the *T* and the *A* as outlined in Chapter 2.4, this study delves into the impact of these factors on the model's age estimation. Specifically, it explores the sensitivity of the age derived from the HL model to variations in *T* and *A*. Furthermore, the *A* from the best model-data match is determined and the related age model is computed as well.

Sensitivity of the HL model-derived age model to varying *T*

In the initial experiment, the *A* was maintained at a constant value of 0.02 m w.e. year^{-1}. The HL model was used to calculate density profiles, incorporating different *T* as variables, which are illustrated in Figure 3.3. The model shows a visible trend where higher *T* facilitate a more rapid progression to higher densities.

Furthermore, the pore close-off density, established at 830 kg m^{-3}, demonstrates a similar temperature-dependent trend. At -40°C, the close-off density is observed at 47.5 m, while at -70 °C, a significantly deeper layer at 193.8 m is required to reach this density, underscoring the influence of temperatures on firn structure and properties. The calculated final densities at the deepest measured point, 204 m deep in core B56, are 917 kg m^{-3} at -40 °C, 916 kg m^{-3} at -50 °C, 903 kg m^{-3} at -60 °C, and 839 kg m^{-3} at -70 °C, respectively. These observations affirm that lower temperatures decelerate the densification process, necessitating deeper layers to reach both critical and close-off densities. It is also noted that as firn approaches its ρ_i (i.e., 917 kg m^{-3}) value, the rate of densification reduces significantly, due to the closure of air pores and the recrystallization processes that constrain further densification.

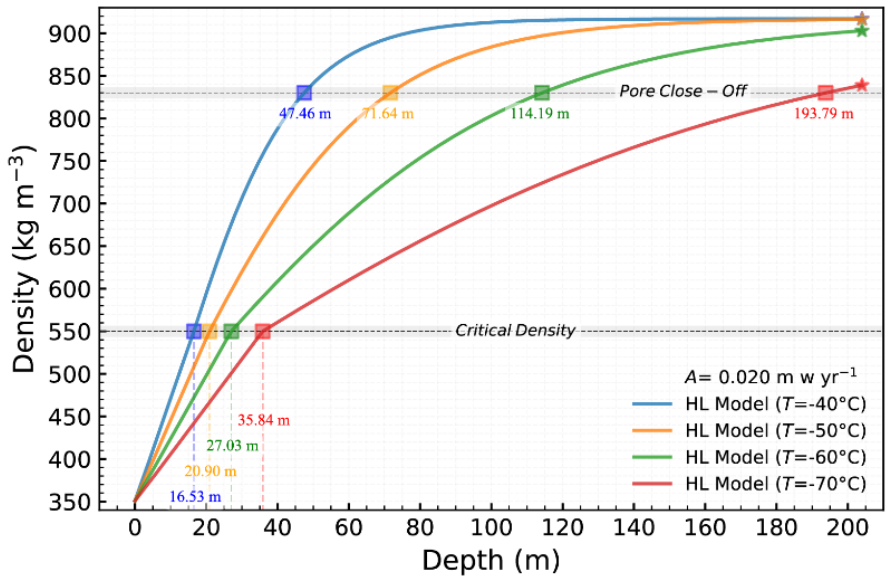

Figure 3.3 : Density profiles generated by the HL model using a constant *A* of 0.02 m w.e. year^{-1} and varying *T*. The colored graphs illustrate the different temperatures used to drive the model. The dark grey dashed line shows the ρ_{550} and the pore close-off density is 830 kg m^{-3}.

These data points suggest that colder temperatures slow down the transformation of firn to ice, thereby requiring a greater depth to reach the ρ_{550} threshold. As the ρ_i value is approached, the rate of densification slows down describing a hysteresis curve.

The resulting age model shows that at shallower depths, the age difference between the models is relatively small; at 60 m, the age difference is within ±200 years (Figure 3.4). This indicates that the densification process near the surface is less sensitive to temperature changes.

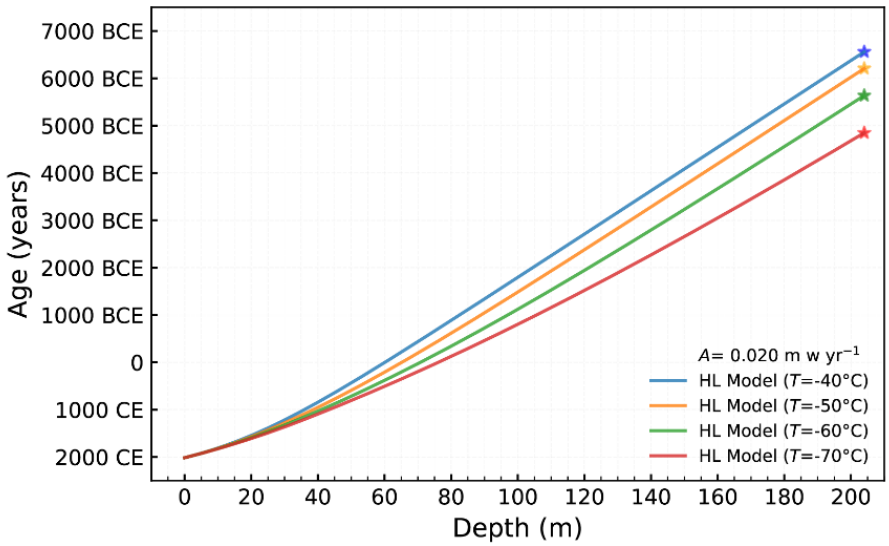

Figure 3.4 : The depth-age relationship as modeled by the HL Model. The colors indicate the different *T* used to drive the model while keeping the *A* constant.

However, as depth increases, the age difference becomes more pronounced, reaching up to ±850 years at a depth of 204 m. This suggests that the impact of temperature variations on age increases more rapidly with depth (Table 3.2).

Table 3.2 : *T*-dependent density variations and timelines derived from the HL model

T (°C)	60 m Density (kg m^{-3}) / year	204 m Density (kg m^{-3}) / year
-40	874 / 5 CE	917 / 6560 BCE
-50	790 / 208 CE	916 / 6208 BCE
-60	689 / 382 CE	903 / 5636 BCE
-70	610 / 508 CE	839 / 4849 BCE

At relatively warmer sites, the ice at a given depth is older than colder sites. This is due to densification and ice formation processes under warmer conditions. The data illustrate that temperature plays a significant role in the rate of ice formation, with higher temperatures leading to older ice at equivalent depths.

Sensitivity of the HL model-derived age model to varying *A*

In the second experiment, the *T* was kept constant at -56°C, while different *A* were used to drive the HL model. Due to the model's setup, which utilizes *T* as the primary driver until the ρ_{550}, the derived density profiles are identical during the first stage of densification (Figure 3.5). Beyond this ρ_{550}, the profiles demonstrate that lower *A* correspond to higher densities at specific depths.

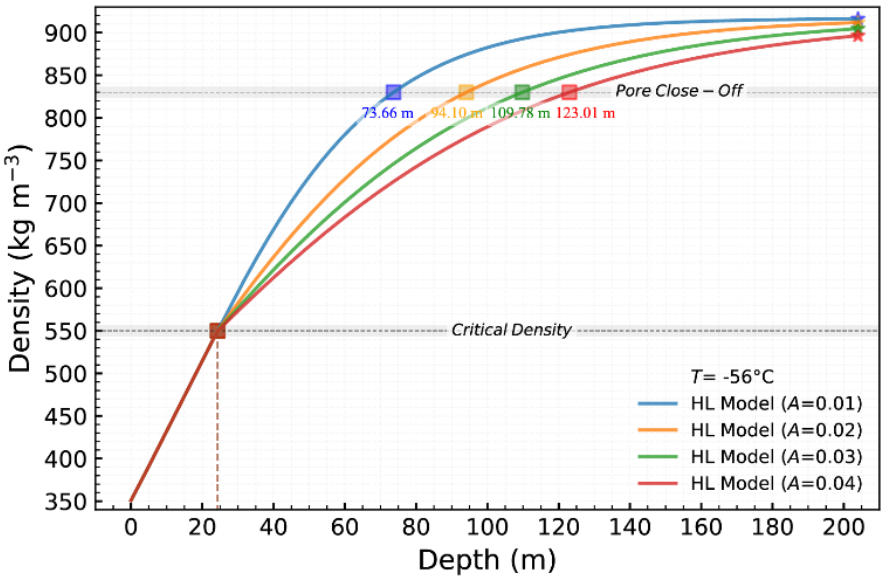

Figure 3.5 : Density profiles generated by the HL model using a constant *T* of -56 °C and varying *A*. The colored graphs illustrate the different accumulation rates used to drive the model. The dark grey dashed line shows that ρ_{550} and the pore close-off density is 830 kg m^{-3}.

At a depth of 204 m, the modeled densities are computed as 916, 912, 905, and 896 kg m^{-3}, corresponding to the input *A* of 0.01, 0.02, 0.03, and 0.04 m w.e. $year^{-1}$, respectively. These results illustrate the competing effects of accumulation rate and *T* on the densification rate. Specifically, a higher densification rate is observed at a lower accumulation rate, yet this rate increases with a higher *T*. Consequently, the comparison of density profiles from different sites indicates that the influence of temperature predominates over the effect of accumulation rate (Hörhold et al., 2011), meaning that sites with warmer temperatures exhibit a higher densification rate (Figure 3.6).

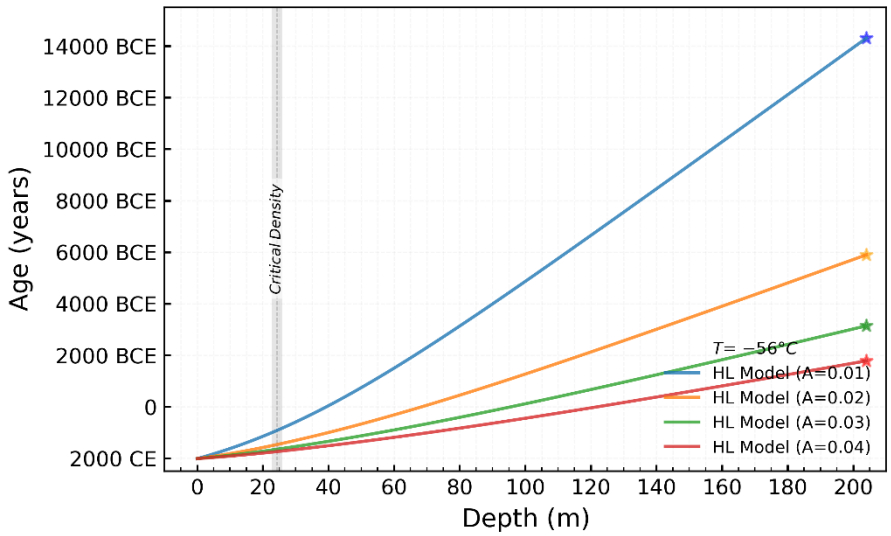

Figure 3.6 : The depth-age relationship as modeled by the HL Model. The colors indicate the different *A* used to drive the model while keeping the *T* constant.

In the model, lower *A* correspond to older ages at specific depths. This may be attributed to the fact that, in areas with low accumulation rates, the layers are thinner, thereby representing longer time intervals (Table 3.3).

Table 3.3 : *A*-dependent density variations and timelines

A (m w.e. $year^{-1}$)	Density (kg m^{-3}) / Year		
	24.3 m	60 m	204 m
0.01	550 / 922 CE	874 / 1495 BCE	917 / 14308 BCE
0.02	550 / 1469 CE	790 / 318 CE	916 / 5896 BCE
0.03	550 / 1651 CE	689 / 903 CE	903 / 3139 BCE
0.04	550 / 1743 CE	610 / 1190 CE	839 / 1780 BCE

This results in older ice at a given depth because less snow accumulates each year, meaning that each m of ice traps more years of snowfall and compaction. Conversely, areas with higher accumulation rates have thicker layers, indicating younger age values. This is because more snow accumulates each year, resulting in thicker layers

that represent fewer years of deposition. According to this model, the rate of accumulation has a significantly greater impact on age determination than temperature.

3.2.2 Age model using the best model - data match

At the B56 site, the on-site *T* of -55.1°C was derived from firn measurements taken at a depth of 10 m (personal communication with Sepp Kipfstuhl). By employing different values of *A*, a series of modeled density profiles were generated to simulate the behavior of the firn under varying conditions. These modeled profiles were compared to the measured bag mean densities (i.e., 1 m average density) of the B56 core. The best match between the data and the model results was obtained to quantify the fit quality (Figure 3.7).

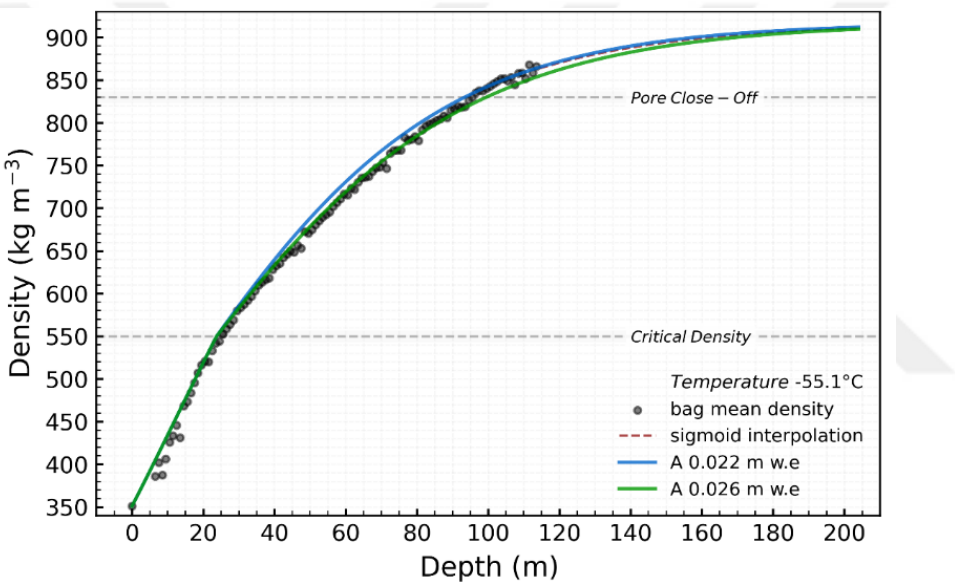

Figure 3.7 : Density model-data match. Gray circles show the measured bag mean density, green and blue lines indicate the modeled density using *A* of 0.022 and 0.026. The dashed red line is a sigmoid interpolation from the last measured bag at 113.5 m to the final depth of the core at 204 m.

According to the HL model, the best fit *A* was identified as approximately 0.024 m w.e. year^{-1}. Reflecting the precision of the measurement and the environmental variability inherent, a 10% tolerance range was applied to this value. This range is defined by a lower limit of approximately 0.022 m w.e. year^{-1}, calculated by subtracting 10% from the 0.024 m w.e. year^{-1} value, and an upper boundary is set at approximately 0.026 m w.e. year^{-1}, calculated by adding a 10% increase to the base value (Figure 3.7). These tolerance limits help ensure that the model remains reliable by accounting for potential variations in environmental conditions and measurement uncertainties.

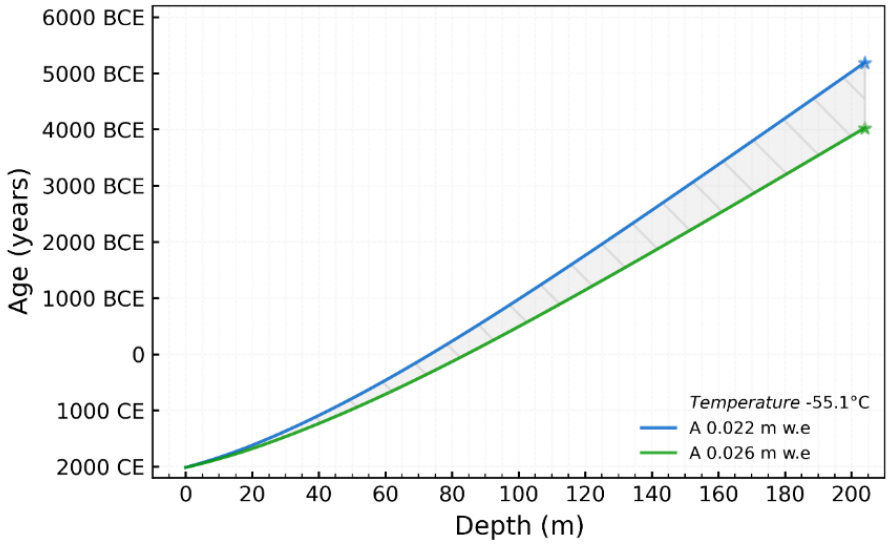

Figure 3.8 : The depth-age relationship as modeled by the HL model. The shaded area highlights the potential variation in age estimation due to differences in *A*. The best-match rates of 0.022 m w.e. year^{-1} and 0.026 m w.e. year^{-1} defined the anticipated age range of the B56 core.

The depth-age relationship, illustrates the significant impact of varying *A* on age estimations. The shaded area represents the potential range of age estimates within the 10% tolerance range applied to the accumulation rate. These values result in an age model (Figure 3.8 is similar to Figure 3.6) characterized by a maximum age variance of approximately ±580 years (Table 3.4).

Table 3.4 : Estimated age ranges as modeled by the HL model

Depth (m)	max Age (years)	min Age (years)	Age range (years)
23.8	1529 CE	1604 CE	±37
204.0	5181 BCE	4019 BCE	±581

This variance is determined by the *A* of 0.022 m w.e. year^{-1}, which corresponds to the maximum age, and 0.026 m w.e. year^{-1}, which corresponds to the minimum age. At a depth of about 204 m, this results in an age estimation ranging between approximately 5200 BCE and 4000 BCE, as detailed in Table 3.4.

3.3 Age Model from Matching Using nssSO_4^{2-} Concentration, and DEP

3.3.1 Matching using nssSO_4^{2-} concentration

In order to derive a list of peaks to match with published and dated peaks of the nssSO_4^{2-} profile, a total of 40 peaks have been identified, as depicted in Figure 3.9.

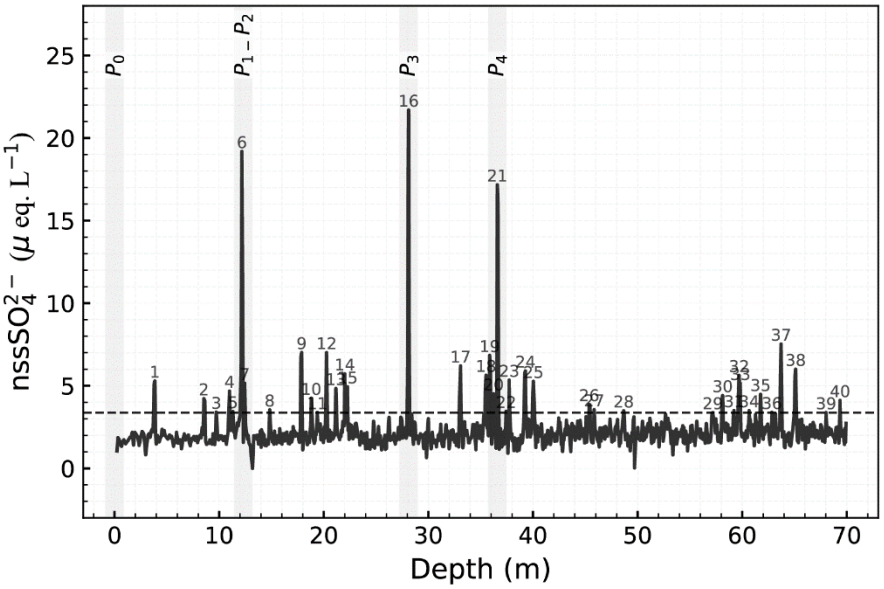

Figure 3.9 : The $nssSO_4^{2-}$ concentration-depth of the B56 core is shown in the figure. The horizontal dashed line shows the threshold value of 3.377 μ eq. L^{-1}. The numbering indicates the single peaks used in this study to match with previously published peaks. Peaks *P_0*, *P_1-P_2*, *P_3*, and *P_4* are absolute age markers, represented and marked by gray bars.

The peaks identified as absolute age markers (Chapter 3.1) have also been identified in the $nssSO_4^{2-}$ profile. Therefore, the names of these peaks were kept to *P_1-P_2*, *P_3*, and *P_4*, and all other $nssSO_4^{2-}$ peaks were denoted by the letter "*S*". Nineteen of the identified peaks were matched to previously published and dated $nssSO_4^{2-}$ profiles by Castellano et al. (2005); Cole-Dai et al. (2000); Igarashi et al. (2011); Longpre et al. (2014); Ren et al. (2010); Stenni et al. (2002), as detailed in Table 3.5.

Regarding the determination of volcanic eruption years and their associated uncertainties, we added uncertainty of +2 years to the deposition times for volcanic events with well-known dates, such as *S_1* meaning Agung 1963 (Self and Rampino, 2012), *S_2* meaning Tarawera 1886 (Hutton, 1887) and Krakatoa 1883 (Self and Rampino, 1981), *S_4* meaning Coseguina 1835 (Scott, 2006), and *S_{14}* meaning Huaynaputina 1600 (Thouret et al., 2002). However, due to the presence of a twin peak in the B56 firn core record for the Tarawera 1886 and Krakatoa 1883 eruptions, the relatively short historical period between these events -proximity of 0.1 m between the layers-, we based our calculations on the earlier Krakatoa event. We added an additional +2 years to the period leading up to the following Tarawera eruption, resulting in a total uncertainty of +5 years for these events. On the other hand, the *S_8* meaning Jorullo volcanic eruption, known to have occurred between 1759 and 1774 (Luhr and Carmichael, 1985), was assigned a date of 1767 ±8.

Table 3.5 : Volcanic events identified in the firn core using $nssSO_4^{2-}$ concentration. [1]This represents the events used as absolute age markers for dating (referred to in Section 3.1), and are compared with volcanic records matched by [2]Castellano et al., (2005), [3]Cole-Dai et al., (2000), [4]Igarashi et al., (2011), [5]Longpre et al., (2014), [6]Ren et al., (2010), and [7]Stenni et al., (2002).

Peaks	$nssSO_4^{2-}$, μ eq L^{-1}	Depth, m	Eruption (CE) and Uncertainty (±), year	Event and Reference
P_0	0.000	00.0	2016	*Snow Surface*
S_1	5.289	03.8	1963 +2	Agung[2,4,5,6]
S_2	4.222	08.5	1883 +5	Tarawera[2,3,4,5,6]
	4.080	08.6		Krakatoa[4]
S_3	3.408	09.7	-	-
S_4	4.680	11.0	1835 +2	Coseguina[3,4,5,6,7]
S_5	3.439	11.3	-	-
P_1	19.190	12.2	1815 +1	Tambora[1]
P_2	5.156	12.5	1809 +2	Unknown 1809[1]
S_8	3.543	14.8	1767 ±8	Jorullo[2]
S_9	7.015	17.9	1693 +2	Unknown 1693[2,3,6,7]
S_{10}	4.249	18.8	1671 +3	PR7[3]
S_{11}	3.385	19.4	-	-
S_{12}	7.011	20.3	-	-
S_{13}	4.834	21.2	-	-
S_{14}	5.723	22.0	1600 +2	Huaynaputina[2,3,4,6,7]
S_{15}	4.942	22.3	1593 +3	PR11[3], 14[4], T15[7]
P_3	21.695	28.3	1453 +4	Kuwae[1]
S_{17}	6.198	33.1	1341 +6	13[2], PR13[3], 18[4], V12[6], T17[7]
S_{18}	5.638	35.5	1285 +4	14[2], PR14[3], 19[4], V13[6], T18[7]
S_{19}	6.836	35.9	1277 +4	PR15[3], 20[4], V14[6], T19[7]
S_{20}	4.519	36.2	1269 +4	15[2], PR16[3], 21[4], T20[7]
P_4	17.168	36.9	1257 +4	Samalas[1]
S_{22}	3.449	37.4	-	-
S_{23}	5.345	37.7	1232 +7	PR18[3], T23[7]
S_{24}	5.900	39.3	-	-
S_{25}	5.269	40.0	-	-
S_{26}	3.871	45.4	-	-
S_{27}	3.555	45.9	-	-
S_{28}	3.488	48.7	-	-
S_{29}	3.379	57.2	-	-
S_{30}	4.413	58.1	-	-
S_{31}	3.505	59.2	-	-
S_{32}	5.630	59.7	765 ±200	22[2]
S_{33}	5.152	59.8	-	-
S_{34}	3.499	60.7	-	-
S_{35}	4.481	61.8	-	-
S_{36}	3.394	62.8	-	-
S_{37}	7.531	63.7	667 ±200	23[2]
S_{38}	6.002	65.1	-	-
S_{39}	3.378	68.0	-	-
S_{40}	4.113	69.4	-	-

Identifying volcanic eruptions with unknown dates was carried out by comparing our data with existing information in the literature. During this process, the dates of volcanic events as reported in other academic studies, along with their specified

uncertainty ranges, were used as the basis (e.g. Castellano et al., 2005; Cole-Dai et al., 2000; Igarashi et al., 2011; Longpre et al., 2014; Ren et al., 2010; Stenni et al., 2002).

An age model is derived from the matching of the 19 peaks, as shown in Figure 3.10, with each peak acting as a tie point; between these, a 95% confidence interval is applied to account for the areas of uncertainty.

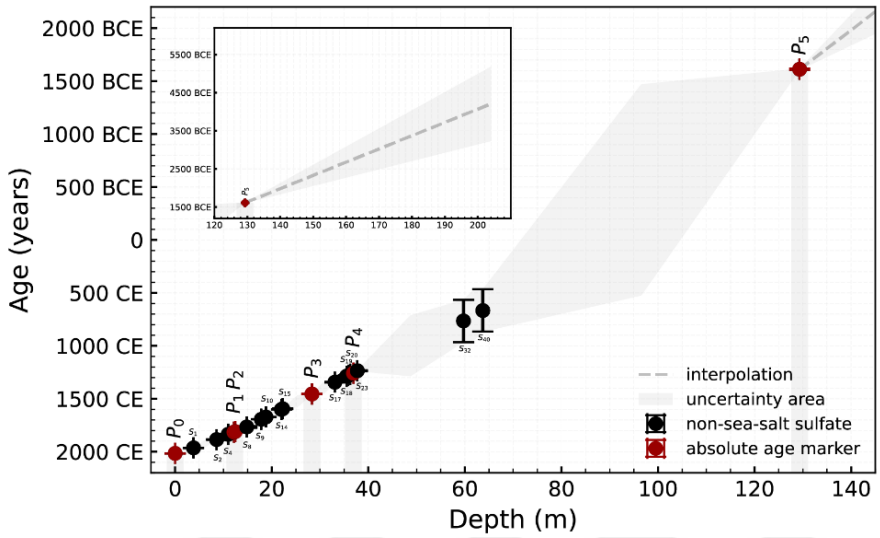

Figure 3.10 : The depth-age relationship obtained by matching of $nssSO_4^{2-}$ peaks. 19 corresponding peaks are represented with black error bars. The red error bar indicates the absolute age markers. Areas of uncertainty are illustrated in grey.

The applied confidence interval indicates that the uncertainty area is affected by both the distance between the identified volcanic eruption events and the amount of uncertainty associated with each eruption. The first 40 m provide a relatively accurate age model due to the abundance of well-documented volcanic eruption dates, resulting in smaller uncertainty areas and a more precise age model.

Beyond 40 m, with increasing depth, matching volcanic eruptions becomes progressively more challenging due to the increasing age and the inherent difficulties in identifying older events. This challenge arises because older volcanic eruptions are typically less well-documented, and the uncertainty in dating these eruptions is higher. Consequently, as depth increases, this issue becomes more pronounced, leading to larger uncertainty intervals for the estimated eruptions.

3.3.2 Matching using DEP

The DEP data were used to apply matching with previously published peaks of both, $nssSO_4^{2-}$ and dielectric properties from literature (Figure 3.11).

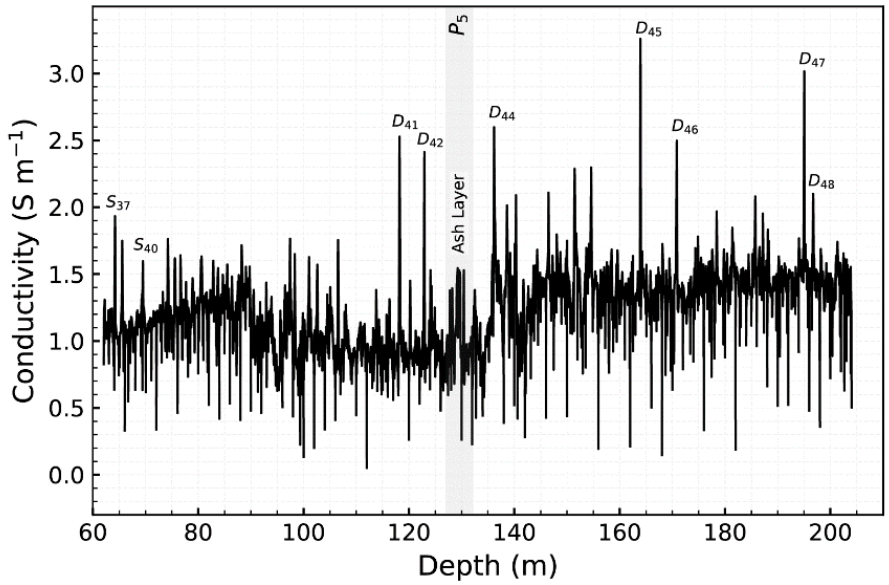

Figure 3.11 : DEP (of conductivity) of the B56 ice core with depth. Peaks represented with "*S*" were matched through nssSO_4^{2-} concentration, while the P_5 peak represents the ash layer used as an absolute age marker. Peaks denoted with "*D*" are selected through matching using the DEP method.

Specifically, the peaks S_{37} and S_{40} have been identified both in the nssSO_4^{2-} concentration data and in the DEP data. Starting from these overlapping peaks, the matching has been extended with the DEP data (Table 3.6).

Table 3.6 : Volcanic events identified in firn core by using DEP. [1]This represents the events used as absolute age markers for dating (referred to in Section 3.1), and are compared with volcanic records matched by [2]Castellano et al., (2005), and [3]Cole-Dai et al., (2000), as well as with the ash layer by [8]Narcisi et al. (2005), [9]Oyabu et al. (2023), and [10]Joe McConnell (unpublished)

Peaks	Conductivity, 10^{-9} S m^{-1}	Depth, m	Eruption (CE) and Uncertainty (±), year	Event and Reference
S_{37}	193.27	64.2	667 ±200 CE	23[2]
S_{40}	159.72	69.4	-	-
D_{41}	252.74	118.2	1218 +7 BCE	PR46[3]
D_{42}	241.29	122.9	1345 +3 BCE	PR47[3]
P_5	-	129.3	1612 ±6 BCE	Ash Layer[8,9,10]
D_{44}	259.80	136.2	1792 ±200 BCE	43[2]
D_{45}	325.91	164.0	2776 ±200 BCE	49[2]
D_{46}	248.28	170.8	3035 ±200 BCE	51[2]
D_{47}	301.52	195.0	3826 ±200 BCE	55[2]
D_{48}	209.86	196.7	3883 ±200 BCE	56[2]

Based on the matching using the DEP data and the absolute age marker P_5, an age model until the final depth of the core was established (Figure 3.12). The P_5 ash layer, located at a depth of 129.3 m, served as a critical reference point, assumed its date is known for sure. This allowed for the precise matching of peaks D_{41}, D_{42}, and D_{44}. This

ash layer was matched with seven peak points corresponding to known volcanic events. Consequently, approximately 197 m of the core were matched with peak points identified in previously published articles.

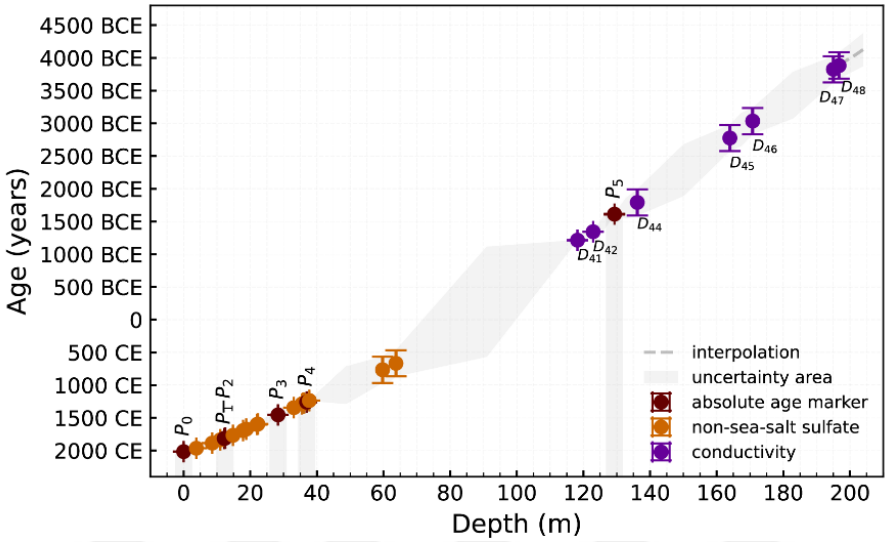

Figure 3.12 : The depth-age relationship as obtained from matching using DEP data. The purple error bars represent the peaks identified from the measured DEP data to match known volcanic events. The orange markers represent peaks matched using $nssSO_4^{2-}$ concentration data. The red markers indicate absolute age markers identified in the core, which are grey columns. In between an uncertainty area was applied. The grey dashed line shows the extrapolated line between the last match point D_{48} and the final depth of 204 m.

At a depth of 197 m, the age was determined to be 3883 ±200 BCE. To estimate the age up to the core's ultimate depth of 204 m, a linear interpolation method was applied. Following this interpolation, the area of uncertainty was calculated. At the final depth of 204 m, the age was approximately estimated to be 4127 BCE ±250 years.

3.3.3 Comparison of the different age models

To establish a reliable chronological framework for the B56 firn core, three age models derived from different methodological approaches were compared: the absolute age markers, the HL model, and the matching using $nssSO_4^{2-}$ concentration, and DEP measurements (Figure 3.13).

The HL model provides a range of possible ages, depending on the accumulation rate which potentially may have changed in the past. It frames the age models from the other approaches.

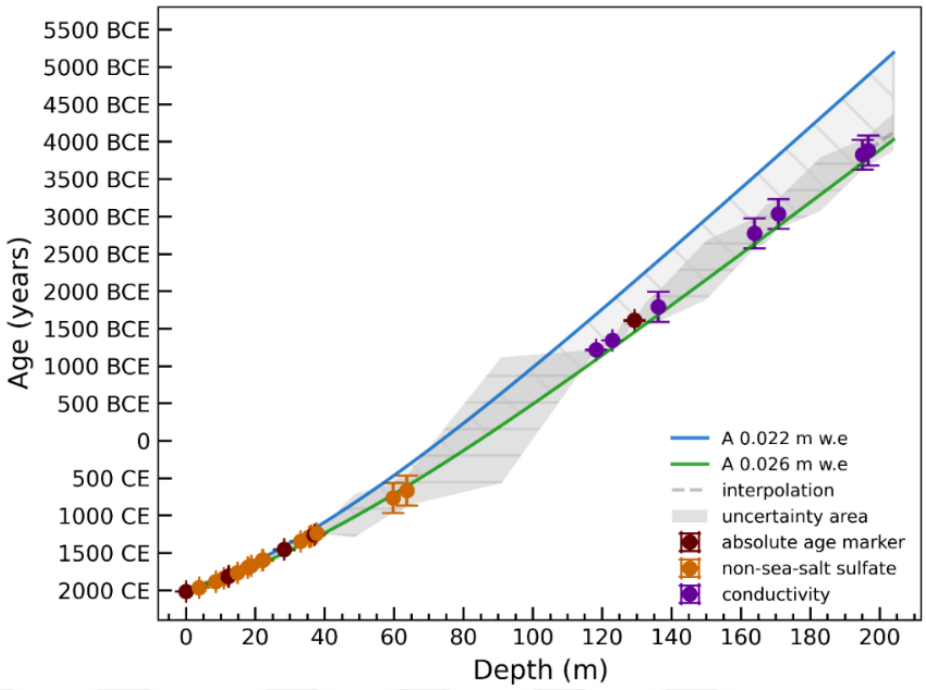

Figure 3.13 : The depth-age relationship as obtained from the three dating approaches. Error bars represent the match points - violet for conductivity, orange for $nssSO_4^{2-}$ and brown for absolute age markers. An uncertainty area was applied between these points. The age range depicted by the green and blue lines is derived from the HL model, which utilizes *A* of 0.022 m w.e. $year^{-1}$ and 0.026 m w.e. $year^{-1}$, respectively. The shaded area shows the potential variation in age estimation due to differences in accumulation rates.

Notably, the age models derived from the matching points, the absolute age markers, and the ash layer show no discernible differences. Therefore, they are merged into one file of tie points (Table 3.7), which can be used as a baseline for the dating of the B56 core and further analysis.

At the maximum depth of 204 m within the firn core, age estimations have been derived from three different models., each providing distinct insight:

- The absolute age markers provide an age of 3930 BCE with an uncertainty of ±970 years (see Figure 3.2).
- The HL model estimates the age to be 4600 BCE, with an uncertainty of ±580 years (see Figure 3.8).
- The age estimated from $nssSO_4^{2-}$ and DEP matching is dated to 4130 BCE, with an associated uncertainty of ±250 years (see for $nssSO_4^{2-}$ Figure 3.10 and for DEP Figure 3.12).

Table 3.7 : Volcanic events identified in the firn core. The peaks of the age model from absolute age markers, $nssSO_4^{2-}$, and DEP are shown by the letter's "*P*", "*S*", and "*D*" respectively. [1]This represents the events used as absolute age markers for dating (referred to in Section 3.1), and are compared with volcanic records matched by [2]Castellano et al., (2005), and [3]Cole-Dai et al., (2000), as well as with the ash layer by [8]Narcisi et al. (2005), [9]Oyabu et al. (2023), and [10]Joe McConnell (unpublished)

Peaks	Depth, m w.e.	Depth, m	HL model Uncertainty (±), year	Eruption	Event and Reference
P_0	00.00	00.00	2016 CE	2016 CE	Snow Surface
S_1	01.34	03.81	1957 ±5	1963 +2 CE	Agung[2,3,5,6]
S_2	03.10	08.58	1877 ±12	1883 +5 CE	Krakatou[4] and Tarawera[2,3,4,5,6]
S_4	04.07	10.99	1833 ±15	1835 +2 CE	Coseguina[3,4,5,6,7]
P_1	04.65	12.33	1808 ±17	1815 +1 CE	Tambora[1]
P_2	04.70	12.46	1806 ±18	1809 +2 CE	Unknown 1809[1]
S_8	05.75	14.83	1760 ±21	1767 ±8 CE	Jorullo[2]
S_9	07.20	17.85	1698 ±27	1693 +2 CE	Unknown 1693[2,3,6,7]
S_{10}	07.67	18.80	1678 ±28	1671 +3 CE	PR7[3]
S_{14}	09.33	22.01	1607 ±34	1600 +2 CE	Huaynaputina[2,3,4,6,7]
S_{15}	09.46	22.27	1602 ±35	1593 +3 CE	PR11[3], 14[4], T15[7]
P_3	12.78	28.33	1460 ±46	1453 +4 CE	Kuwae[1]
S_{17}	15.54	33.08	1343 ±57	1341 +6 CE	13[2], PR13[3], 18[4], V12[6], T17[7]
S_{18}	17.00	35.51	1281 ±62	1285 +4 CE	14[2], PR14[3], 19[4], V13[6], T18[7]
S_{19}	17.23	35.89	1271 ±63	1277 +4 CE	PR15[3], 20[4], V14[6], T19[7]
S_{20}	17.44	36.23	1262 ±64	1269 +4 CE	15[2], PR16[3], 21[4], T20[7]
P_4	17.86	36.92	1244 ±65	1257 +4 CE	Samalas[1]
S_{23}	18.35	37.73	1223 ±67	1232 +7 CE	PR18[3], T23[7]
S_{32}	32.97	59.71	600 ±123	765 ±200 CE	22[2]
S_{37}	35.86	63.72	477 ±134	667 ±200 CE	23[2]
D_{41}	80.02	118.22	1381 ±303	1218 +7 BCE	PR46[3]
D_{42}	84.11	122.91	1551 ±318	1345 +3 BCE	PR47[3]
P_5	89.73	129.32	1787 ±339	1612 ±6 BCE	Ash Layer[8,9,10]
D_{44}	95.78	136.17	2039 ±361	1792 ±200 BCE	43[2]
D_{45}	120.61	163.95	3079 ±451	2776 ±200 BCE	49[2]
D_{46}	126.78	170.81	3338 ±474	3035 ±200 BCE	51[2]
D_{47}	148.68	195.03	4258 ±552	3826 ±200 BCE	55[2]
D_{48}	150.22	196.73	4323 ±558	3883 ±200 BCE	56[2]

The three age models derived from the three different approaches are very compatible with each other (Figure 3.13). This indicates that the derived age models give a reasonable result.

4. DISCUSSION

4.1 Time Series of Accumulation Rate

The identification of 27 different volcanic events by matching nssSO_4^{2-} concentration and DEP enables the prediction of accumulation rate time series. The *A* is calculated using equation 4.1:

$$A = \frac{\Delta d}{\Delta t} \tag{4.1}$$

where Δd represents the change in depth, measured in m w.e., and Δt denotes the time interval in years between two consecutive measurements. This formula facilitates the determination of accumulation rates by quantifying the depth changes over time intervals marked by volcanic events within the firn core (Figure 4.1).

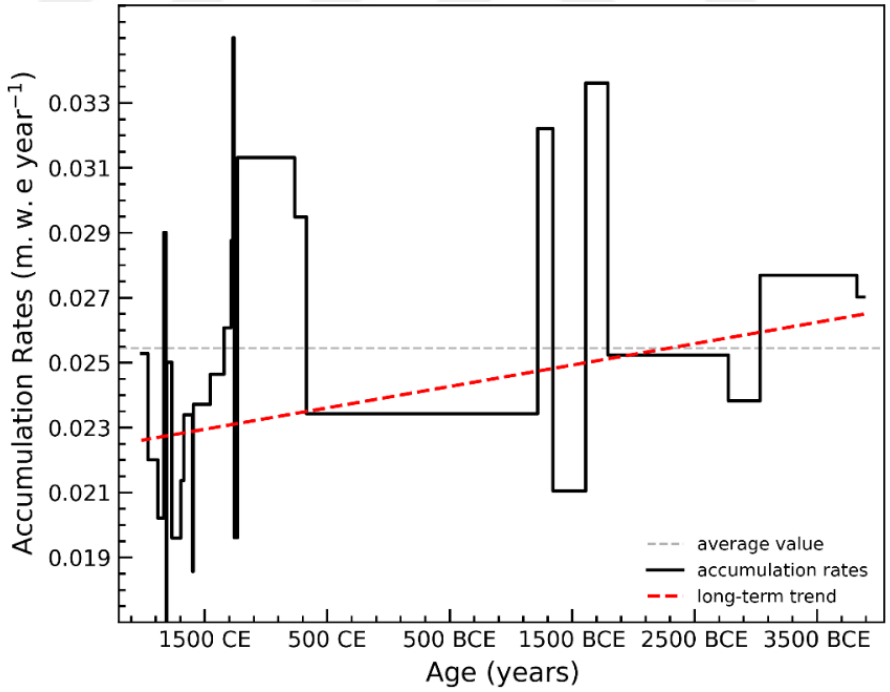

Figure 4.1 : Shows the accumulation rates inferred from depth-age data obtained from the B56 firn core. The horizontal dashed grey line represents the average accumulation rate of 0.0254 m w.e. year^{-1}. Additionally, the red dashed line depicts the long-term trend in accumulation rates.

The time series of accumulation rates presented in Table 4.1 provides a chronological record of the accumulation history of the B56 firn core. This table shows changes in accumulation rates over different time periods based on specific geological events such as volcanic eruptions.

Table 4.1 : Time series of accumulation rates

Time Series, years			Average accumulation rates, m w.e. $year^{-1}$
2016 CE	-	1963 CE	0.0253
1963 CE	-	1883 CE	0.0220
1883 CE	-	1835 CE	0.0202
1835 CE	-	1815 CE	0.0290
1815 CE	-	1809 CE	0.0083
1809 CE	-	1767 CE	0.0250
1767 CE	-	1693 CE	0.0196
1693 CE	-	1671 CE	0.0214
1671 CE	-	1600 CE	0.0234
1600 CE	-	1593 CE	0.0186
1593 CE	-	1453 CE	0.0237
1453 CE	-	1341 CE	0.0246
1341 CE	-	1285 CE	0.0261
1285 CE	-	1277 CE	0.0288
1277 CE	-	1269 CE	0.0263
1269 CE	-	1257 CE	0.0350
1257 CE	-	1232 CE	0.0196
1232 CE	-	765 CE	0.0313
765 CE	-	667 CE	0.0295
667 CE	-	1218 BCE	0.0234
1218 BCE	-	1345 BCE	0.0322
1345 BCE	-	1612 BCE	0.0210
1612 BCE	-	1792 BCE	0.0336
1792 BCE	-	2776 BCE	0.0252
2776 BCE	-	3035 BCE	0.0238
3035 BCE	-	3826 BCE	0.0277
3826 BCE	-	3883 BCE	0.0270

The *A* in the Dome Fuji region and its surroundings have been determined to range between 0.020 and 0.030 m w.e. $year^{-1}$, as evidenced by previous studies (Anschütz et al., 2011; Igarashi et al., 2011; Oyabu et al., 2023). Analysis conducted for the B56 firn core, utilizing the $nssSO_4^{2-}$ concentration, and DEP method for volcanic eruption matching, indicates an average accumulation rate of 0.025 m w.e. $year^{-1}$. Additionally, the HL model is the best fit at an average accumulation rate of 0.024 m w.e. $year^{-1}$. These findings demonstrate the consistency in average accumulation rates for the Dome Fuji region and its surrounding areas.

4.2 Usage of the HL Model as a Dating Tool

The depth-age relationship illustrated by the HL model is compared with the outcomes derived from volcanic event matching (see Figure 4.2). The graph demonstrates a certain level of consistency between the two methodologies as depth increases over time; however, it also reveals variations in age estimations at specific depths. While the HL model estimates an age of 4550 BCE ± 580 years (see Figure 3.8) at a depth of 204 m, the volcanic matching model suggests an age of 4130 BCE ± 250 years (see Figure 3.12) for the same depth.

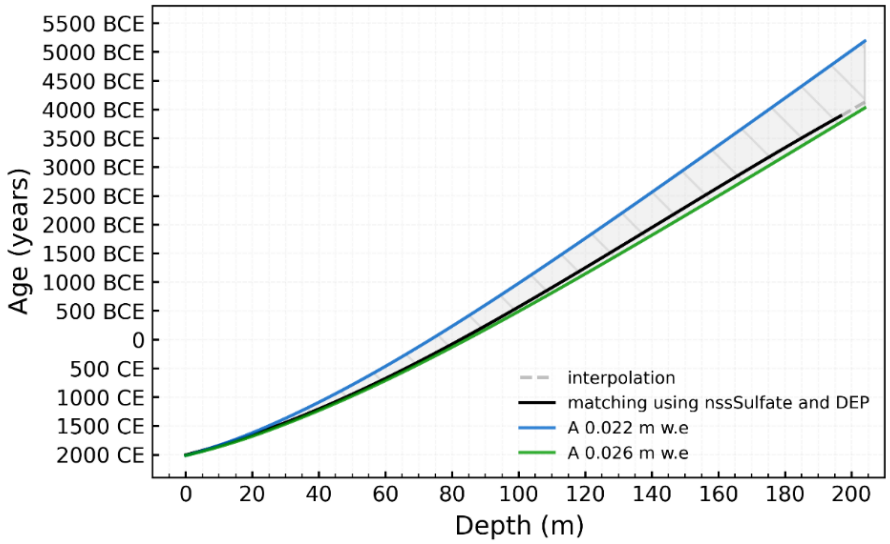

Figure 4.2 : A comparison of the model derived using the HL model with best-fit value against the model obtained from the matching of volcanic events.

Within the framework of these models, it is evident that the HL model presumes constant *T* and *A*, which, while facilitating a practical and rapid dating process, overlooks the complex dynamics exhibited by glacial systems over time. This approach tends to increase uncertainties, particularly for deeper ice layers. Moreover, the use of constant accumulation rates by this model does not provide information on the annual accumulation trends of the glacier.

Conversely, the volcanic matching model is based on distinct stratigraphic markers, specifically identified volcanic ash layers and chemical signatures within the ice core. This method is generally more effective in determining the age of ice for certain periods, often with a narrower margin of uncertainty. However, the process of identifying and correlating accurate volcanic signals in complex and remote regions such as East Antarctica is exceedingly laborious. Additionally, volcanic matching

faces reliability issues for older time periods due to the absence of precise dating of volcanic events.

The combined use of both models serves to balance the limitations of a single approach and offers a more comprehensive framework for dating. Such a synthesis is complementary, providing crucial data for understanding past changes and informing future climate models.

4.3 Comparison of B56 Firn Core to Other Firn Cores

When the positional proximity of ice core samples B54 and B55 to sample B56 is considered, the similarity in their age-depth relationship suggests that the regional climatic conditions and snow accumulation processes recorded by these samples are quite comparable (see Figure 2.1). This similarity also extends to the EDC (AICC23) (Bouchet et al., 2023) and DF1 (from Dome F) cores (Oyabu et al. 2023), which have age profiles that correlate with depth, indicating similar accumulation rates (Figure 4.3).

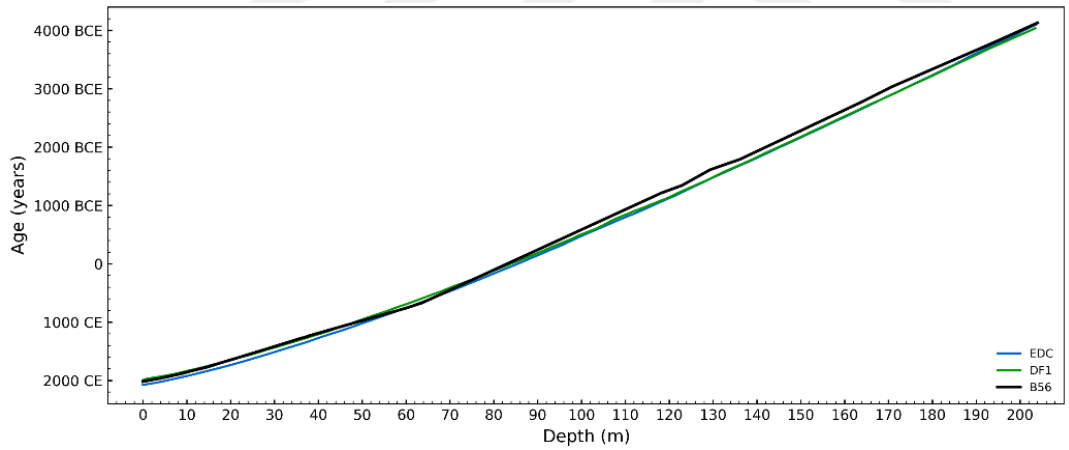

Figure 4.3 : This graph shows the B56 core's depth-age relationship in comparison to other cores. The black line represents the B56 firn core, which was derived by matching $nssSO_4^{2-}$ and DEP data. The blue line represents the EPICA Dome C AICC23 core, while the green line represents the DF1 core from Dome F.

On the other hand, compared with samples B51, B53, and especially B40, the accumulation amount and temperatures indicated by sample B56 are much lower relative to coastal regions.

5. CONCLUSION

This study presents a chronology of the B56 firn core from the EAP using three different dating methods: absolute age markers, the HL model, and $nssSO_4^{2-}$ concentrations / DEP.

Five absolute age markers were identified: Tambora (P_1), the 1809 "Unknown" (P_2), Kuwae (P_3), Samalas (P_4), and an ash layer (P_5). The HL model was applied using a ρ_0 of 0.351 m w.e. year^{-1} and a T of -55.1 °C measured in the field. $nssSO_4^{2-}$ were used for the first 70 m and matched with 17 volcanic eruptions; DEP was used from 70 m to the bottom of the core -204 m- and matched with 7 volcanic events. The results provide insights into historical climate conditions and accumulation rates over approximately six thousand years.

Using absolute age markers, the bottom of the core is dated to approximately 3932 BCE ±973 years (see Figure 3.2). In contrast, the HL model estimates this depth to be around 4600 BCE ±580 years (see Figure 3.8), and the $nssSO_4^{2-}$ and DEP method dates it to approximately 4130 BCE ±250 years (see Figure 3.12). Absolute age markers provide precise dates but are limited to identifiable volcanic events. HL model assumes constant climatic conditions, giving an older age estimate that might be higher due to its assumptions. The $nssSO_4^{2-}$ and DEP methods provide higher resolution data, resulting in dates between the other two methods, but with increasing uncertainty at greater depths due to the complexity of matching volcanic events.

The accumulation rates derived from absolute age markers are as follows:

- P_0 - P_1 (2016-1815 CE): 0.0231 m w.e. year^{-1}
- P_1 - P_2 (1815-1809 CE): 0.0083 m w.e. year^{-1}
- P_2 - P_3 (1809-1453 CE): 0.0227 m w.e. year^{-1}
- P_3 - P_4 (1453-1257 CE): 0.0259 m w.e. year^{-1}
- P_4 - P_5 (1257 CE-1612 BCE): 0.0251 m w.e. year^{-1}

The overall average accumulation rate for absolute age markers is 0.0247 m w.e. year^{-1}. The HL model found the best fit to the bag mean density data at 0.024 m w.e. year^{-1}, with an optimum accumulation rate of ±0.002 m w.e. year^{-1} and a tolerance range of 10% for this value (see Figure 3.8), closely matching the overall average rate from absolute age markers. In contrast, the nssSO_4^{2-} and DEP method shows a slightly higher average rate of 0.0254 m w.e. year^{-1} (see Table 4.1 and Figure 4.1). This higher accumulation rate might be due to the increased sensitivity and resolution of the nssSO_4^{2-} and DEP methods in identifying annual accumulation layers.

Absolute age markers are highly precise for dating specific volcanic events but are limited to identifiable volcanic events. The HL model uses density profiles to estimate age and is useful for quickly obtaining ages, but it relies on the assumption of constant climate conditions, which may not reflect historical variations. The nssSO_4^{2-} and DEP methods provide high-resolution data but the complexity and uncertainty increase with depth as matching volcanic events becomes more difficult.

These findings provide important information about past climate conditions and ice accumulation processes on the East Antarctic Plateau. Using different dating methods together creates a reliable timeline and serves as a valuable reference for future research.

REFERENCES

Alley, R. B. (1987). Firn densification by grain-boundary sliding: A first model. *Journal de Physique. Colloque*, *48*(C1), C1-256. https://doi.org/10.1051/jphyscol:1987135.

Alley, R. B. (1988). Concerning the Deposition and Diagenesis of Strata in Polar Firn. *Journal of Glaciology*, *34*(118), 283–290. https://doi.org/10.1017/s0022143000007024.

Alley, R. B., Shuman, C. A., Meese, D. A., Gow, A. J., Taylor, K. C., Cuffey, K. M., ... Grootes P. M. (1997). Visual-stratigraphic dating of the GISP2 ice core: Basis, reproducibility, and application. *Journal of Geophysical Research: Oceans*, *102*(C12), 26367–26381. https://doi.org/10.1029/96jc03837.

Anschütz, H., Sinisalo, A., Isaksson, E., McConnell, J. R., Hamran, S. E., Bisiaux, M. M., … Pasteris, D. (2011). Variation of accumulation rates over the last eight centuries on the East Antarctic Plateau derived from volcanic signals in ice cores. *Journal of Geophysical Research*, *116*(D20). https://doi.org/10.1029/2011jd015753.

Arnaud, L., Barnola, J. M., and Duval, P. (2000). Physical modeling of the densification of snow/firn and ice in the upper part of polar ice sheets. *Physics of Ice Core Records*, 285–305. hdl.handle.net/2115/32472.

Aronson, R. B., Thatje, S., McClintock, J. B., and Hughes, K. A. (2011). Anthropogenic impacts on marine ecosystems in Antarctica. *Annals of the New York Academy of Sciences*, *1223*(1), 82–107. https://doi.org/10.1111/j.1749-6632.2010.05926.x.

Barnola, J. M., Pimienta, P., Raynaud, D., and Korotkevich, Y. S. (1991). CO_2-climate relationship as deduced from the Vostok ice core: a re-examination based on new measurements and on a re-evaluation of the air dating. *Tellus B*, *43*(2), 83–90. https://doi.org/10.1034/j.1600-0889.1991.t01-1-00002.x.

Barrett, P. (2003). Cooling a continent. *Nature*, *421*(6920), 221–223. https://doi.org/10.1038/421221a.

Barrett, P. (2008). A History of Antarctic Cenozoic Glaciation – View from the Margin. *Developments in Earth and Environmental Sciences*, 33–83. https://doi.org/10.1016/s1571-9197(08)00003-7.

Barry, R., and Gan, T. Y. (2011). Ice sheets. *The Global Cryosphere: Past, Present and Future*. Cambridge University Press, 138–164. https://doi.org/10.1017/cbo9780511977947.006.

Bender, M., Sowers, T., and Brook, E. (1997). Gases in ice cores. *Proceedings of the National Academy of Sciences*, *94*(16), 8343–8349. https://doi.org/10.1073/pnas.94.16.8343.

Bénédicte, L. D., Eric, B., Jean-Robert, P., Claire, W., Anders, S., Catherine, …. Frédéric, P. (2010). Corrigendum to "Consistent dating for Antarctic and Greenland ice cores" *Quaternary Science Reviews*, *29*(19–20), 2821–2822. https://doi.org/10.1016/j.quascirev.2010.06.025.

Bertler, N. A. N. (2011). Ice Core. *Encyclopedia of Earth Sciences Series*, *Encyclopedia of Snow, Ice and Glaciers*, 584–589. https://doi.org/10.1007/978-90-481-2642-2_260.

Bijl, P. K., Bendle, J. a. P., Bohaty, S. M., Pross, J., Schouten, S., Tauxe, L., …. Yamane, M. (2013). Eocene cooling linked to early flow across the Tasmanian Gateway. *Proceedings of the National Academy of Sciences*, *110*(24), 9645–9650. https://doi.org/10.1073/pnas.1220872110.

Bindschadler, R. A., Alley, R. B., Anderson, J., Shipp, S., Borns, H., Fastook, J. …. Shuman, C. A. (1998). What is happening to the West Antarctic Ice Sheet? *Eos, Transactions American Geophysical Union*, *79*(22), 257–265. https://doi.org/10.1029/98eo00188.

Bo, S., Siegert, M. J., Mudd, S. M., Sugden, D., Fujita, S., Xiangbin, C., …. Yuansheng, L. (2009). The Gamburtsev mountains and the origin and early evolution of the Antarctic Ice Sheet. *Nature*, *459*(7247), 690–693. https://doi.org/10.1038/nature08024.

Boger, S. D. (2011). Antarctica — Before and after Gondwana. *Gondwana Research*, *19*(2), 335–371. https://doi.org/10.1016/j.gr.2010.09.003.

Bohleber, P., Roman, M., Barbante, C., Vascon, S., Siddiqi, K., and Pelillo, M. (2021). Ice Core Science Meets Computer Vision: Challenges and Perspectives. *Frontiers in Computer Science*, *3*, 2624-9898. https://doi.org/10.3389/fcomp.2021.690276.

Bouchet, M., Landais, A., Grisart, A., Parrenin, F., Prié, F., Jacob, R., …. Yang, G. (2023). The Antarctic Ice Core Chronology 2023 (AICC2023) chronological framework and associated timescale for the European Project for Ice Coring in Antarctica (EPICA) Dome C ice core. *Climate of the Past*, *19*(11), 2257–2286. https://doi.org/10.5194/cp-19-2257-2023.

Budd, W. F., McInnes, B. J., Jenssen, D., and Smith, I. N. (1987). Modelling the response of the West Antarctic ice sheet to a climatic warming. *Dynamics of the West Antarctic Ice Sheet. Glaciology and Quaternary Geology*, 321–358. https://doi.org/10.1007/978-94-009-3745-1_17.

Buizert, C. (2013). Ice Core Methods | Studies of firn air. *Encyclopedia of Quaternary Science*, 361–372. https://doi.org/10.1016/b978-0-444-53643-3.00330-7.

Castellano, E., Becagli, S., Hansson, M., Hutterli, M., Petit, J. R., Rampino, M. R. …. Udisti, R. (2005). Holocene volcanic history as recorded in the sulfate stratigraphy of the European Project for Ice Coring in Antarctica Dome C (EDC96) ice core. *Journal of Geophysical Research Atmospheres: Atmospheres*, *110*(D6). https://doi.org/10.1029/2004jd005259.

Cole-Dai, J., Ferris, D., Lanciki, A., Savarino, J., Baroni, M., and Thiemens, M. H. (2009). Cold decade (AD 1810–1819) caused by Tambora (1815) and another (1809) stratospheric volcanic eruption. *Geophysical Research Letters*, *36*(22). https://doi.org/10.1029/2009gl040882.

Cole-Dai, J., Mosley-Thompson, E., Wight, S. P., and Thompson, L. G. (2000). A 4100-year record of explosive volcanism from an East Antarctica ice core. *Journal of Geophysical Research: Atmospheres*, *105*(D19), 24431–24441. https://doi.org/10.1029/2000jd900254.

Craig, H. (1961). Isotopic variations in meteoric waters. *Science*, *133*(3465), 1702–1703. https://doi.org/10.1126/science.133.3465.1702.

Cuffey, K. M., and Vimeux, F. (2001). Covariation of carbon dioxide and temperature from the Vostok ice core after deuterium-excess correction. *Nature*, *412*(6846), 523–527. https://doi.org/10.1038/35087544.

Cui, X., Sun, B., Tian, G., Tang, X., Zhang, X., Jiang, Y., Guo, J., and Li, X. (2009). Ice radar investigation at Dome A, East Antarctica: Ice thickness and subglacial topography. *Chinese Science Bulletin*, *55*(4–5), 425–431. https://doi.org/10.1007/s11434-009-0546-z.

Dalziel, I. W. D., and Elliot, D. H. (1982). West Antarctica: Problem child of Gondwanaland. *Tectonics*, *1*(1), 3–19. https://doi.org/10.1029/tc001i001p00003.

Dansgaard, W., Clausen, H. B., Gundestrup, N., Hammer, C. U., Johnsen, S. F., Kristinsdottir, P. M., and Reeh, N. (1982). A new Greenland deep ice core. *Science*, *218*(4579), 1273–1277. https://doi.org/10.1126/science.218.4579.1273.

Dansgaard, W., Johnsen, S. J., Møller, J., and Langway, C. C. (1969). One Thousand Centuries of Climatic Record from Camp Century on the Greenland Ice Sheet. *Science*, *166*(3903), 377–381. https://doi.org/10.1126/science.166.3903.377.

Davies, B. J., Hambrey, M. J., Smellie, J. L., Carrivick, J. L., and Glasser, N. F. (2012). Antarctic Peninsula Ice Sheet evolution during the Cenozoic Era. *Quaternary Science Reviews*, *31*, 30–66. https://doi.org/10.1016/j.quascirev.2011.10.012.

DeBeer, C. M., Sharp, M., and Schuster-Wallace, C. (2020). Glaciers and ice sheets. *Reference Module in Earth Systems and Environmental Sciences*, 182–194. https://doi.org/10.1016/b978-0-12-409548-9.12441-8.

DeConto, R. M., and Pollard, D. (2016). Contribution of Antarctica to past and future sea-level rise. *Nature*, *531*(7596), 591–597. https://doi.org/10.1038/nature17145.

Delmas, R. J. (1992). Environmental information from ice cores. *Reviews of Geophysics*, *30*(1), 1–21. https://doi.org/10.1029/91rg02725.

Ding, M., Xiao, C., Yang, Y., Wang, Y., Li, C., Yuan, N. …. Ming, J. (2016). Re-assessment of recent (2008–2013) surface mass balance over Dome Argus, *Antarctica. Polar Research*, *35*(1), 26133. https://doi.org/10.3402/polar.v35.26133.

Dittmann, A., Schlosser, E., Masson-Delmotte, V., Powers, J. G., Manning, K. W., Werner, M., and Fujita, K. (2016). Precipitation regime and stable isotopes at Dome Fuji, East Antarctica. *Atmospheric Chemistry and Physics*, *16*(11), 6883–6900. https://doi.org/10.5194/acp-16-6883-2016.

Ehlers, J., and Gibbard, P. L. (2007). The extent and chronology of Cenozoic Global Glaciation. *Quaternary International*, *164*, 6–20. https://doi.org/10.1016/j.quaint.2006.10.008.

Elias, S. (2021). Greenland ice sheet. *Threats to the Arctic*, 265–321. https://doi.org/10.1016/b978-0-12-821555-5.00009-7.

Faria, S. H., Kipfstuhl, S., and Lambrecht, A. (2017). *The EPICA-DML deep ice core: A visual record*, Springer, 9–22. https://doi.org/10.1007/978-3-662-55308-4_2.

Faure, G., and Mensing, T. M. (2010). The East Antarctic ice Sheet. *The Transantarctic Mountains*, 573–633. https://doi.org/10.1007/978-90-481-9390-5_17.

Fischer, H., Fundel, F., Ruth, U., Twarloh, B., Wegner, A., Udisti, R., …. Wagenbach, D. (2007). Reconstruction of millennial changes in dust emission, transport and regional sea ice coverage using the deep EPICA ice cores from the Atlantic and Indian Ocean sector of Antarctica. *Earth and Planetary Science Letters*, *260*(1–2), 340–354. https://doi.org/10.1016/j.epsl.2007.06.014.

Fisher, D. A., Reeh, N., and Clausen, H. (1985). Stratigraphic Noise in Time Series Derived from Ice Cores. Annals of Glaciology, *7*, 76–83. https://doi.org/10.3189/s0260305500005942.

Fowler, A. (2003). Glaciers. *Encyclopedia of Atmospheric Sciences*, 869–875. https://doi.org/10.1016/b0-12-227090-8/00158-5.

Francis, J., Marenssi, S., Levy, R., Hambrey, M., Thorn, V., Mohr, B., …. DeConto, R. (2008). Chapter 8 From Greenhouse to Icehouse – The Eocene/Oligocene in Antarctica. *In Developments in earth and environmental sciences*, 309–368. https://doi.org/10.1016/s1571-9197(08)00008-6.

Freitag, J., Wilhelms, F., and Kipfstuhl, S. (2004). Microstructure-dependent densification of polar firn derived from X-ray microtomography. *Journal of Glaciology*, *50*(169), 243–250. https://doi.org/10.3189/172756504781830123.

Frezzotti, M., Pourchet, M., Flora, O., Gandolfi, S., Gay, M., Urbini, S., …. Fily, M. (2005). Spatial and temporal variability of snow accumulation in East Antarctica from traverse data. *Journal of Glaciology*, *51*(172), 113–124. https://doi.org/10.3189/172756505781829502.

Gabrielli, P., and Vallelonga, P. (2015). Contaminant Records in Ice Cores. *Developments in Paleoenvironmental Research*, 393–430. https://doi.org/10.1007/978-94-017-9541-8_14.

Gao, C., Robock, A., Self, S., Witter, J. B., Steffenson, J. P., Clausen, H. B., …. Ammann, C. (2006). The 1452 or 1453 A.D. Kuwae eruption signal derived from multiple ice core records: Greatest volcanic sulfate event of the past 700 years. *Journal of Geophysical Research Atmospheres*, *111*(D12). https://doi.org/10.1029/2005jd006710.

González, S., Vasallo, F., Sanz, P., Quesada, A., and Justel, A. (2021). Characterization of the summer surface mesoscale dynamics at Dome F, Antarctica. *Atmospheric Research*, *259*, 105699. https://doi.org/10.1016/j.atmosres.2021.105699.

Goujon, C., Barnola, J., and Ritz, C. (2003). Modeling the densification of polar firn including heat diffusion: Application to close-off characteristics and gas isotopic fractionation for Antarctica and Greenland sites. *Journal of Geophysical Research Atmospheres*, *108*(D24). https://doi.org/10.1029/2002jd003319.

Graham, A. G. C. (2011). Ice sheet. Encyclopedia of snow, ice and glaciers. *Encyclopedia of earth sciences*, 592–608. https://doi.org/10.1007/978-90-481-2642-2_277.

Greve, R., and Blatter, H. (2009). Ice in the Climate System. *Advances in Geophysical and Environmental Mechanics and Mathematics*, 1–6. https://doi.org/10.1007/978-3-642-03415-2_1.

Grootes, P. M., Stuiver, M., White, J. W. C., Johnsen, S., and Jouzel, J. (1993). Comparison of oxygen isotope records from the GISP2 and GRIP Greenland ice cores. *Nature*, *366*(6455), 552–554. doi.org:10.1038/366552a0.

Hambrey, M., and Glasser, N. (2005). Sedimentary Processes | Glaciers. *Encyclopedia of Geology*, 663–678. https://doi.org/10.1016/b0-12-369396-9/00169-6.

Hammer, C. U., Clausen, H. B., and Dansgaard, W. (1980). Greenland ice sheet evidence of post-glacial volcanism and its climatic impact. *Nature*, *288*(5788), 230–235. https://doi.org/10.1038/288230a0.

Hanna, E., Navarro, F. J., Pattyn, F., Domingues, C. M., Fettweis, X., Ivins, E. R. …. Zwally, H. J. (2013). Ice-sheet mass balance and climate change. *Nature*, *498*(7452), 51–59. https://doi.org/10.1038/nature12238.

Hawkesworth, C., Kelley, S., Turner, S., Roex, A. L., and Storey, B. (1999). Mantle processes during Gondwana break-up and dispersal. *Journal of African Earth Sciences*, *28*(1), 239–261. https://doi.org/10.1016/s0899-5362(99)00026-3.

Herron, M. M., Herron, S. L., and Langway, C. C. (1981). Climatic signal of ice melt features in southern Greenland. *Nature*, *293*(5831), 389–391. https://doi.org/10.1038/293389a0.

Herron, M. M., and Langway, C. C. (1980). Firn Densification: an Empirical model. *Journal of Glaciology*, *25*(93), 373–385. https://doi.org/10.3189/s0022143000015239.

Hofstede, C. M., Van De Wal Roderik, S., Kaspers, K. A., Van Den Broeke, M. R., Karlöf, L., Winther, J. …. Wilhelms, F. (2004). Firn accumulation records for the past 1000 years on the basis of dielectric profiling of six cores from Dronning Maud Land, *Antarctica. Journal of Glaciology*, *50*(169), 279–291. https://doi.org/10.3189/172756504781830169.

Hondoh, T., Shoji, H., Watanabe, O., Salamatin, A. N., and Lipenkov, V. Y. (2002). Depth–age and temperature prediction at Dome Fuji station, East Antarctica. *Annals of Glaciology*, 35, 384–390. https://doi.org/10.3189/172756402781817013.

Hörhold, M., Laepple, T., Freitag, J., Bigler, M., Fischer, H., and Kipfstuhl, S. (2012). On the impact of impurities on the densification of polar firn. *Earth and Planetary Science Letters*, 325–326, 93–99. https://doi.org/10.1016/j.epsl.2011.12.022.

Hörhold, M. W., Kipfstuhl, S., Wilhelms, F., Freitag, J., and Frenzel, A. (2011). The densification of layered polar firn. *Journal of Geophysical Research Atmospheres, 116*(F1). https://doi.org/10.1029/2009jf001630.

Houben, A. J. P., Bijl, P. K., Sluijs, A., Schouten, S., and Brinkhuis, H. (2019). Late Eocene Southern Ocean cooling and invigoration of circulation preconditioned Antarctica for Full-Scale glaciation. *Geochemistry Geophysics Geosystems, 20*(5), 2214–2234. https://doi.org/10.1029/2019gc008182.

Hutton, F. W. (1887). The eruption of Mount Tarawera. *Quarterly Journal of the Geological Society*, *43*(1–4), 178–189. https://doi.org/10.1144/gsl.jgs.1887.043.01-04.16.

Huybrechts, P. (1994). Formation and disintegration of the Antarctic ice sheet. *Annals of Glaciology*, 20, 336–340. https://doi.org/10.3189/1994aog20-1-336-340.

Igarashi, M., Nakai, Y., Motizuki, Y., Takahashi, K., Motoyama, H., and Makishima, K. (2011). Dating of the Dome Fuji shallow ice core based on a record of volcanic eruptions from AD 1260 to AD 2001. *Polar Science, 5*(4), 411–420. https://doi.org/10.1016/j.polar.2011.08.001.

Johnsen, S. J., Dansgaard, W., Clausen, H. B., and Langway, C. C. (1972). Oxygen Isotope Profiles through the Antarctic and Greenland Ice Sheets. *Nature, 235*(5339), 429–434. https://doi.org/10.1038/235429a0.

Jokat, W., Boebel, T., König, M., and Meyer, U. (2003). Timing and geometry of early Gondwana breakup. *Journal of Geophysical Research, 108*(B9). https://doi.org/10.1029/2002jb001802.

Joughin, I., and Alley, R. B. (2011). Stability of the West Antarctic ice sheet in a warming world. *Nature Geoscience*, *4*(8), 506–513. https://doi.org/10.1038/ngeo1194.

Joughin, I., Smith, B. E., and Medley, B. (2014). Marine ice sheet collapse potentially under way for the Thwaites Glacier basin, West Antarctica. *Science*, *344*(6185), 735–738. https://doi.org/10.1126/science.1249055.

Jouzel, J., Masson-Delmotte, V., Cattani, O., Dreyfus, G., Falourd, S., Hoffmann, G. …. Wolff, E. W. (2007). Orbital and Millennial Antarctic Climate Variability over the Past 800,000 Years. *Science*, *317*(5839), 793–796. https://doi.org/10.1126/science.1141038.

Jouzel, J., and Merlivat, L. (1984). Deuterium and oxygen 18 in precipitation: Modeling of the isotopic effects during snow formation. *Journal of Geophysical Research*, *89*(D7), 11749–11757. https://doi.org/10.1029/jd089id07p11749.

Karlöf, L., Winther, J., Isaksson, E., Kohler, J., Pinglot, J. F., Wilhelms …. Van De Wal, R. S. W. (2000). A 1500 year record of accumulation at Amundsenisen western Dronning Maud Land, Antarctica, derived from electrical and radioactive measurements on a 120 m ice core. *Journal of Geophysical Research Atmospheres*, *105*(D10), 12471–12483. https://doi.org/10.1029/1999jd901119.

Koerner, R. M. (1997). Some comments on climatic reconstructions from ice cores drilled in areas of high melt. *Journal of Glaciology*, *43*(143), 90–97. https://doi.org/10.3189/s0022143000002847.

Lavigne, F., Degeai, J., Komorowski, J., Guillet, S., Robert, V., Lahitte, P. …. De Belizal, E. (2013). Source of the great A.D. 1257 mystery eruption unveiled, Samalas volcano, Rinjani Volcanic Complex, Indonesia. *Proceedings of the National Academy of Sciences*, *110*(42), 16742–16747. https://doi.org/10.1073/pnas.1307520110.

Legrand, M., and Mayewski, P. (1997). Glaciochemistry of polar ice cores: A review. *Reviews of Geophysics*, *35*(3), 219–243. https://doi.org/10.1029/96rg03527.

Longpré, M., Stix, J., Burkert, C., Hansteen, T., and Kutterolf, S. (2014). Sulfur budget and global climate impact of the A.D. 1835 eruption of Cosigüina volcano, Nicaragua. *Geophysical Research Letters*, *41*(19), 6667–6675. https://doi.org/10.1002/2014gl061205.

Lottes, A. L., and Rowley, D. B. (1990). Reconstruction of the Laurasian and Gondwanan segments of Permian Pangaea. *Memoirs of the Geological Society of London*, *12*(1), 383–395. https://doi.org/10.1144/gsl.mem.1990.012.01.36.

Lowe, D. J. (2011). Tephrochronology and its application: A review. *Quaternary Geochronology*, *6*(2), 107–153. https://doi.org/10.1016/j.quageo.2010.08.003.

Luhr, J. F., and Carmichael, I. S. E. (1985). Jorullo Volcano, Michoacán, Mexico (1759–1774): The earliest stages of fractionation in calc-alkaline magmas. *Contributions to Mineralogy and Petrology*, *90*(2–3), 142–161. https://doi.org/10.1007/bf00378256.

Lundin, J. M., Stevens, C. M., Arthern, R., Buizert, C., Orsi, A., Ligtenberg, S. R. …. Waddington, E. (2017). Firn Model Intercomparison Experiment (FirnMICE). *Journal of Glaciology*, *63*(239), 401–422. https://doi.org/10.1017/jog.2016.114.

Mackintosh, A. N., Verleyen, E., O'Brien, P. E., White, D. A., Jones, R. S., McKay …. Masse, G. (2014). Retreat history of the East Antarctic Ice Sheet since the Last Glacial Maximum. *Quaternary Science Reviews*, *100*, 10–30. https://doi.org/10.1016/j.quascirev.2013.07.024.

Masson-Delmotte, V., Kageyama, M., Braconnot, P., Charbit, S., Krinner, G., Ritz, C. …. Yu, Y. (2005). Past and future polar amplification of climate change: climate model intercomparisons and ice-core constraints. *Climate Dynamics*, *26*(5), 513–529. https://doi.org/10.1007/s00382-005-0081-9.

Mayewski, P. A., Meeker, L. D., Whitlow, S., Twickler, M. S., Morrison, M. C., Alley, R. B. …. Taylor, K. (1993). The atmosphere during the younger Dryas. *Science*, *261*(5118), 195–197. https://doi.org/10.1126/science.261.5118.195.

Mayewski, P. A., Meeker, L. D., Whitlow, S., Twickler, M. S., Morrison, M. C., Bloomfield, P. …. Wumkes, W. (1994). Changes in Atmospheric Circulation and Ocean Ice Cover over the North Atlantic During the Last 41,000 Years. *Science*, *263*(5154), 1747–1751. https://doi.org/10.1126/science.263.5154.1747.

Merlivat, L., and Jouzel, J. (1979). Global climatic interpretation of the deuterium-oxygen 18 relationship for precipitation. *Journal of Geophysical Research Atmospheres*, *84*(C8), 5029–5033. https://doi.org/10.1029/jc084ic08p05029.

Moore, J. C., Narita, H., and Maeno, N. (1991). A continuous 770-year record of volcanic activity from east Antarctica. *Journal of Geophysical Research*, *96*(D9), 17353–17359. https://doi.org/10.1029/91jd01283

Motoyama, H. (2007). The second deep ice coring project at Dome Fuji, Antarctica. *Scientific Drilling*, *5*, 41–43. https://doi.org/10.2204/iodp.sd.5.05.2007.

Narcisi, B., Petit, J., Delmonte, B., Basile-Doelsch, I., and Maggi, V. (2005). Characteristics and sources of tephra layers in the EPICA-Dome C ice record (East Antarctica): Implications for past atmospheric circulation and ice core stratigraphic correlations. *Earth and Planetary Science Letters*, *239*(3–4), 253–265. https://doi.org/10.1016/j.epsl.2005.09.005.

Narcisi, B., Petit, J. R., Delmonte, B., Batanova, V., and Savarino, J. (2019). Multiple sources for tephra from AD 1259 volcanic signal in Antarctic ice cores. *Quaternary Science Reviews*, *210*, 164–174. https://doi.org/10.1016/j.quascirev.2019.03.005.

Naughten, K. A., Holland, P. R., and De Rydt, J. (2023). Unavoidable future increase in West Antarctic ice-shelf melting over the twenty-first century. *Nature Climate Change*, *13*(11), 1222–1228. https://doi.org/10.1038/s41558-023-01818-x.

Oerter, H., Wilhelms, F., Jung-Rothenhäusler, F., Göktas, F., Miller, H., Graf, W., and Sommer, S. (2000). Accumulation rates in Dronning Maud Land, Antarctica, as revealed by dielectric-profiling measurements of shallow firn cores. *Annals of Glaciology*, *30*, 27–34. https://doi.org/10.3189/172756400781820705.

Oppenheimer, M. (1998). Global warming and the stability of the West Antarctic Ice Sheet. *Nature*, *393*(6683), 325–332. https://doi.org/10.1038/30661.

Otosaka, I. N., Horwath, M., Mottram, R., and Nowicki, S. (2023). Mass Balances of the Antarctic and Greenland Ice Sheets Monitored from Space. *Surveys in Geophysics*, *44*(5), 1615–1652. https://doi.org/10.1007/s10712-023-09795-8.

Oyabu, I., Kawamura, K., Buizert, C., Parrenin, F., Orsi, A., Kitamura …. Nakazawa, T. (2022). The Dome Fuji ice core DF2021 chronology (0–207 kyr BP). *Quaternary Science Reviews*, *294*, 107754. https://doi.org/10.1016/j.quascirev.2022.107754.

Oyabu, I., Kawamura, K., Fujita, S., Inoue, R., Motoyama, H., Fukui, K. …. Yoshimori, M. (2023). Temporal variations of surface mass balance over the last 5000 years around Dome Fuji, Dronning Maud Land, East Antarctica. *Climate of the Past*, *19*(2), 293–321. https://doi.org/10.5194/cp-19-293-2023.

Parrenin, F., Barnola, J., Beer, J., Blunier, T., Castellano, E., Chappellaz, J. …. Wolff, E. W. (2007). The EDC3 chronology for the EPICA Dome C ice core. *Climate of the Past*, *3*(3), 485–497. https://doi.org/10.5194/cp-3-485-2007.

Parrenin, F., Dreyfus, G., Durand, G., Fujita, S., Gagliardini, O., Gillet, F. …. Yoshida, N. (2007). 1-D-ice flow modelling at EPICA Dome C and Dome Fuji, East Antarctica. *Climate of the Past*, *3*(2), 243–259. https://doi.org/10.5194/cp-3-243-2007.

Paterson, W. S. B. (1994). *The Physics of glaciers* (3rd Edition). Pergamon. https://doi.org/10.1016/C2009-0-14802-X.

Petit, J., and Raynaud, D. (2020). Forty years of ice-core records of CO_2. *Nature*, *579*(7800), 505–506. https://doi.org/10.1038/d41586-020-00809-8.

Pinti, D. (2011). *Antarctica*. Encyclopedia of Astrobiology. https://doi.org/10.1007/978-3-642-11274-4_83.

Pinti, D. (2015). *Antarctica*. Encyclopedia of Astrobiology. https://doi.org/10.1007/978-3-662-44185-5_83.

Raible, C. C., Brönnimann, S., Auchmann, R., Brohan, P., Frölicher, T. L., Graf, H. …. Wegmann, M. (2016). Tambora 1815 as a test case for high impact volcanic eruptions: Earth system effects. Wiley Interdisciplinary Reviews. *Climate Change*, *7*(4), 569–589. https://doi.org/10.1002/wcc.407.

Ren, J., Li, C., Hou, S., Xiao, C., Qin, D., Li, Y., and Ding, M. (2010). A 2680 year volcanic record from the DT-401 East Antarctic ice core. *Journal of Geophysical Research Atmospheres*, *115*(D11). https://doi.org/10.1029/2009jd012892.

Rignot, E., Mouginot, J., Morlighem, M., Seroussi, H., and Scheuchl, B. (2014). Widespread, rapid grounding line retreat of Pine Island, Thwaites, Smith, and Kohler glaciers, West Antarctica, from 1992 to 2011. *Geophysical Research Letters*, *41*(10), 3502–3509. https://doi.org/10.1002/2014gl060140.

Rignot, E., Velicogna, I., Van Den Broeke, M. R., Monaghan, A., and Lenaerts, J. T. M. (2011). Acceleration of the contribution of the Greenland and Antarctic ice sheets to sea level rise. *Geophysical Research Letters*, *38*(5). https://doi.org/10.1029/2011gl046583.

Ritz, C., Rommelaere, V., and Dumas, C. (2001). Modeling the evolution of Antarctic ice sheet over the last 420,000 years: Implications for altitude changes in the Vostok region. *Journal of Geophysical Research Atmospheres*, *106*(D23), 31943–31964. https://doi.org/10.1029/2001jd900232.

Saruya, T., Fujita, S., Iizuka, Y., Miyamoto, A., Ohno, H., Hori, A. …. Goto-Azuma, K. (2022). Development of crystal orientation fabric in the Dome Fuji ice core in East Antarctica: implications for the deformation regime in ice sheets. *The Cryosphere*, *16*(7), 2985–3003. https://doi.org/10.5194/tc-16-2985-2022.

Scambos, T. A., Campbell, G. G., Pope, A., Haran, T., Muto, A., Lazzara …. Van Den Broeke, M. R. (2018). Ultralow surface temperatures in East Antarctica from satellite thermal infrared mapping: The coldest places on Earth. *Geophysical Research Letters*, *45*(12), 6124–6133. https://doi.org/10.1029/2018gl078133.

Scambos, T. A., Bell, R. E., Alley, R. B., Anandakrishnan, S., Bromwich, D. H., Brunt, K. …. Yager, P. L. (2017). How much, how fast?: A science review and outlook for research on the instability of Antarctica's Thwaites Glacier in the 21st century. *Global and Planetary Change*, *153*, 16–34. https://doi.org/10.1016/j.gloplacha.2017.04.008.

Scherer, R. P. (1991). Quaternary and Tertiary microfossils from beneath Ice Stream B: Evidence for a dynamic West Antarctic Ice Sheet history. *Global and Planetary Change*, *4*(4), 395–412. https://doi.org/10.1016/0921-8181(91)90005-h.

Scott, W., Gardner, C., Devoli, G., and Alvarez, A. (2006). The A.D. 1835 eruption of Volcán Cosigüina, Nicaragua: A guide for assessing local volcanic hazards. *Volcanic Hazards in Central America | GeoScienceWorld*. https://doi.org/10.1130/2006.2412(09).

Self, S., and Rampino, M. R. (1981). The 1883 eruption of Krakatau. *Nature*, *294*(5843), 699–704. https://doi.org/10.1038/294699a0.

Self, S., and Rampino, M. R. (2012). The 1963–1964 eruption of Agung volcano (Bali, Indonesia). *Bulletin of Volcanology*, *74*(6), 1521–1536. https://doi.org/10.1007/s00445-012-0615-z.

Shepherd, A., Ivins, E. R., Velicogna, I., Broeke, M., Whitehouse, P., Joughin, I. …. Wouters, B. (2018). Mass balance of the Antarctic Ice Sheet from 1992 to 2017. *Nature*, *558*(7709), 219–222. https://doi.org/10.1038/s41586-018-0179-y.

Siegert, M., Hein, A. S., White, D. A., Gore, D. B., De Santis, L., and Hillenbrand, C. (2022). Antarctic Ice Sheet changes since the Last Glacial Maximum. *Antarctic Climate Evolution (Second Edition)*, 623–687. https://doi.org/10.1016/b978-0-12-819109-5.00002-5.

Siegert, M. J. (2003). Glacial–interglacial variations in central East Antarctic ice accumulation rates. *Quaternary Science Reviews*, *22*(5–7), 741–750. https://doi.org/10.1016/s0277-3791(02)00191-9.

Sigl, M., Winstrup, M., McConnell, J. R., Welten, K. C., Plunkett, G., Ludlow, F. …. Woodruff, T. E. (2015). Timing and climate forcing of volcanic eruptions for the past 2,500 years. *Nature*, *523*(7562), 543–549. https://doi.org/10.1038/nature14565.

Smellie, J. L., Haywood, A. M., Hillenbrand, C., Lunt, D. J., and Valdes, P. J. (2009). Nature of the Antarctic Peninsula Ice Sheet during the Pliocene: Geological evidence and modelling results compared. *Earth-science Reviews*, *94*(1–4), 79–94. https://doi.org/10.1016/j.earscirev.2009.03.005.

Spencer, M. K., Alley, R. B., and Creyts, T. T. (2001). Preliminary firn-densification model with 38-site dataset. *Journal of Glaciology*, *47*(159), 671–676. https://doi.org/10.3189/172756501781831765.

Stenni, B., Proposito, M., Gragnani, R., Flora, O., Jouzel, J., Falourd, S., and Frezzotti, M. (2002). Eight centuries of volcanic signal and climate change at Talos Dome (East Antarctica). *Journal of Geophysical Research Atmospheres*, *107*(D9). https://doi.org/10.1029/2000jd000317.

Stokes, C. R., Abram, N. J., Bentley, M. J., Edwards, T. L., England, M. H., Foppert, A. …. Whitehouse, P. L. (2022). Response of the East Antarctic Ice Sheet to past and future climate change. *Nature*, *608*(7922), 275–286. https://doi.org/10.1038/s41586-022-04946-0.

Storey, B. C., and Granot, R. (2021). Chapter 1.1 Tectonic history of Antarctica over the past 200 million years. *Memoirs of the Geological Society of London*, *55*(1), 9–17. https://doi.org/10.1144/m55-2018-38.

Stothers, R. B. (1984). The Great Tambora eruption in 1815 and its aftermath. *Science*, *224*(4654), 1191–1198. https://doi.org/10.1126/science.224.4654.1191.

Stump, E., and Fairbridge, R. W. (2006). Antarctica. World Regional Geology. *Encyclopedia of Earth Science Series*, 2–14. https://doi.org/10.1007/3-540-31081-1_2.

Svensson, A. (2015). Ice cores. Encyclopedia of Scientific Dating Methods. *Encyclopedia of Earth Sciences Series*, 341–348. https://doi.org/10.1007/978-94-007-6304-3_159.

Thomas, E. R., Van Wessem, J. M., Roberts, J., Isaksson, E., Schlosser, E., Fudge, T. J. …. Ekaykin, A. A. (2017). Regional Antarctic snow accumulation over the past 1000 years. *Climate of the Past*, *13*(11), 1491–1513. https://doi.org/10.5194/cp-13-1491-2017.

Thomas, R. H. (1979). Ice Shelves: A review. *Journal of Glaciology, 24*(90), 273–286. https://doi.org/10.3189/s0022143000014799.

Thompson, L. G., Yao, T., Mosley-Thompson, E., Davis, M. E., Henderson, K. A., and Lin, P. (2000). A High-Resolution Millennial Record of the South Asian Monsoon from Himalayan Ice Cores. *Science, 289*(5486), 1916–1919. https://doi.org/10.1126/science.289.5486.1916.

Thouret, J. C., Juvigné, E., Gourgaud, A., Boivin, P., and Dávila, J. (2002). Reconstruction of the AD 1600 Huaynaputina eruption based on the correlation of geologic evidence with early Spanish chronicles. *Journal of Volcanology and Geothermal Research, 115*(3–4), 529–570. https://doi.org/10.1016/s0377-0273(01)00323-7.

Van Der Veen, C. J. (1987). The West Antarctic ice Sheet: the need to understand its dynamics. Dynamics of the West Antarctic Ice Sheet. *Glaciology and quaternary geology*, 1–16. https://doi.org/10.1007/978-94-009-3745-1_1.

Van Liefferinge, B., Taylor, D., Tsutaki, S., Fujita, S., Gogineni, P., Kawamura, K. …. Sugiura, K. (2021). Surface mass balance controlled by local surface slope in inland Antarctica: Implications for Ice-Sheet mass balance and oldest ice delineation in Dome Fuji. *Geophysical Research Letters, 48*(24). https://doi.org/10.1029/2021gl094966.

Vaughan, D. (2006). Recent Trends in Melting Conditions on the Antarctic Peninsula and Their Implications for Ice-Sheet Mass Balance and Sea Level. *Arctic, Antarctic, and Alpine Research, 38*(1), 147–152. https://doi.org/10.1657/1523-0430(2006)038 .

Vaughan, D. G., and Doake, C. S. M. (1996). Recent atmospheric warming and retreat of ice shelves on the Antarctic Peninsula. *Nature, 379*(6563), 328–331. https://doi.org/10.1038/379328a0.

Veevers, J. (2004). Gondwanaland from 650–500 Ma assembly through 320 Ma merger in Pangea to 185–100 Ma breakup: supercontinental tectonics via stratigraphy and radiometric dating. *Earth-science Reviews, 68*(1–2), 1–132. https://doi.org/10.1016/j.earscirev.2004.05.002.

Waddington, E., and Lingle, C. (2013). Ice Cores | Dynamics of the East Antarctic Ice Sheet. *Encyclopedia of Quaternary Science*, 456–462. https://doi.org/10.1016/b978-0-444-53643-3.00031-5.

Walker, M. J. C., Berkelhammer, M., Björck, S., Cwynar, L. C., Fisher, D. A., Long, A. J. …. Weiss, H. (2012). Formal subdivision of the Holocene Series/Epoch: a Discussion Paper by a Working Group of Intimate (Integration of ice-core, marine and terrestrial records) and the Subcommission on Quaternary Stratigraphy (International Commission on Stratigraphy). *Journal of Quaternary Science, 27*(7), 649–659. https://doi.org/10.1002/jqs.2565.

Wang, Y., Sodemann, H., Hou, S., Masson-Delmotte, V., Jouzel, J., and Pang, H. (2012). Snow accumulation and its moisture origin over Dome Argus, Antarctica. *Climate Dynamics, 40*(3–4), 731–742. https://doi.org/10.1007/s00382-012-1398-9.

Weinhart, A. H., Freitag, J., Hörhold, M., Kipfstuhl, S., and Eisen, O. (2020). Representative surface snow density on the East Antarctic Plateau. *The Cryosphere*, *14*(11), 3663–3685. https://doi.org/10.5194/tc-14-3663-2020.

Witter, J. B., and Self, S. (2006). The Kuwae (Vanuatu) eruption of AD 1452: potential magnitude and volatile release. *Bulletin of Volcanology*, *69*(3), 301–318. https://doi.org/10.1007/s00445-006-0075-4.

Wolff, E., Barbante, C., Becagli, S., Bigler, M., Boutron, C., Castellano, E. …. Wegner, A. (2010). Changes in environment over the last 800,000 years from chemical analysis of the EPICA Dome C ice core. *Quaternary Science Reviews*, *29*(1–2), 285–295. https://doi.org/10.1016/j.quascirev.2009.06.013.

Xiao, C., Li, Y., Hou, S., Allison, I., Bian, L., and Ren, J. (2008). Preliminary evidence indicating Dome A (Antarctica) satisfying preconditions for drilling the oldest ice core. *Chinese Science Bulletin*, *53*(1), 102–106. https://doi.org/10.1007/s11434-007-0520-6.

Zhai, Z., Wang, Y., Reijmer, C. H., Smeets, P. C. J. P., Zhang, X., and Zhang, W. (2024). MODIS land surface temperature in East Antarctica: accuracy and its main affecting factors. *Journal of Glaciology*, 1–31. https://doi.org/10.1017/jog.2024.17.

Zielinski, G. A. (2000). Use of paleo-records in determining variability within the volcanism–climate system. *Quaternary Science Reviews*, *19*(1–5), 417–438. https://doi.org/10.1016/s0277-3791(99)00073-6.

Zielinski, G. A., Mayewski, P. A., Meeker, L. D., Whitlow, S., Twickler, M. S., Morrison, M. …. Alley, R. B. (1994). Record of Volcanism Since 7000 B.C. from the GISP2 Greenland Ice Core and Implications for the Volcano-Climate System. *Science*, *264*(5161), 948–952. https://doi.org/10.1126/science.264.5161.948.

Zwally, H. J., and Jun, L. (2002). Seasonal and interannual variations of firn densification and ice-sheet surface elevation at the Greenland summit. *Journal of Glaciology*, *48*(161), 199–207. https://doi.org/10.3189/172756502781831403.

CURRICULUM VITAE

Name Surname **:** Furkan Kaan Sağol

EDUCATION **:**

- **B.Sc.** **:** 2020, Atatürk University, Faculty of Earth Sciences, Petroleum and Natural Gas Engineering

PROFESSIONAL EXPERIENCE AND REWARDS:

- February 2023-June 2023: Istanbul Technical University, Geomorphology and Cosmogenic Nuclides Laboratory, Research Assistant
- May 2022-November 2022: Istanbul Technical University, Scientific Research Projects, Research Assistant

PUBLICATIONS, PRESENTATIONS AND PATENTS ON THE THESIS:

- **Sagol, F.K.**, Schwamborn, G., Freitag, J., Kipfstuhl, S., Wilhelms, F., and Hörhold, M. 2024: Dating and interpreting a firn core from the East Antarctic Plateau. EGU General Assembly, April 14-19, 2024, Vienna, Austria. https://doi.org/10.5194/egusphere-egu24-15484.